39th European Rotorcraft Forum, Moscow, 3-6 September, 2013 - Paper 90

NUMERICAL STUDY OF ROTORS IN SHIP AIRWAKE

C. Crozon, R. Steijl and G.N. Barakos

CFD Laboratory, School of Engineering
University of Liverpool, L69 3GH, U.K.
http://www.liv.ac.uk/flightscience/PROJECTS/CFD/ROTORCRAFT/RBD/index.htm
Email: crozon@liverpool.ac.uk, rsteijl@liverpool.ac.uk, G.Barakos@liverpool.ac.uk

Abstract

Operating helicopters in a naval environment is challenging as it imposes a pilot workload significantly higher than during land-based operations. The aerodynamic interaction between the aircraft and the ship wake is known to play an important role in increasing the pilot workload, hence reducing the safety of maritime helicopter missions. As a further step towards numerical prediction of Ship Helicopter Operational Limitations (SHOL), CFD simulations are conducted on the Canadian Patrol Frigate (CPF). The effect of the rotor is added to the simulation, first using an actuator disk method together with steady calculations, then using fully-articulated rotor blades and the URANS equations. Results using the actuator disk method demonstrate the importance of coupling effects when the rotor is operating closely to the ship and therefore the invalidity of superposition methods. The case of a Sea-King helicopter main rotor hovering above the deck just before touchdown is reproduced to overcome the limitations of steady calculations and the actuator disk method. Predictions of rotor thrust correlate with the experimental data available and give confidence in the results. The findings highlight the differences in rotor loading between forward flight and near-deck operation.

The possibility of using CFD for the simulation of freely-flying aircraft by integrating a flight-mechanics model into HMB is part of the future work.

NOMENCLATURE

Ω_{mag}	Vorticity magnitude
μ	Rotor advance ratio
Ψ	Rotor azimuth
$\tilde{u}$	Velocity pertubation
$\underline{u}$	Velocity vector $\underline{u} = [u, v, w]^T$
b	Ship beam length
C_T^{UK}	UK Rotor thrust coefficient $\frac{T}{\frac{1}{2}\rho U_{tip}^2 \pi R^2}$
P^*	Dimensionless pressure
T	Rotor thrust
U	Mean value of flow velocity
U_∞	Rotor advance speed
U_{tip}	Rotor blade tip speed
$\vec{F_i}$, $\vec{F_v}$	Inviscid and viscous fluxes
$\mathbf{R}_{i,j,k}$	Flux residuals at cell (i, j, k)
$\vec{S}$	Source term
$\vec{u}_h$	Local velocity field in the rotor-fixed frame of reference
$V(t)$	Time dependent control volume
$\mathbf{w}_{i,j,k}$	Discretised conserved variables vector
$\vec{\mathbf{w}}$	Conserved variables vector
ρ	Air density
$\vec{\omega}$	Rotor rotational speed
WOD	Wind Over Deck angle.
CPF	Canadian Patrol Frigate
DES	Detached Eddy Simulation
DI	Dynamic Interface
Green wind	Wind from starboard
LES	Large Eddy Simulation
LHA	Landing Helicopter Assault
Red wind	Wind from portside
SFS	Simple Frigate Shape
SHOL	Ship Helicopter Operational Limitations

1 INTRODUCTION

Operating helicopters in a naval environment poses challenging problems as it increases the pilot workload to levels not normally encountered during land-based operations [17]. The size of the landing spot, the boat motion, the airwake unsteadiness, weather and lighting conditions are some of the factors that add to the pilot workload and may turn the take-off and recovery procedures impossible to complete. The ship airwake is a combination of the wind and ship motion, and is influenced by the atmospheric boundary layer and globally any element of the boat superstructure. It usually shows a very unsteady behaviour, with characteristic frequencies below 2Hz, while a pilot consciously responds to frequencies in the range of 0.2 to 1.6Hz [39]. The ship aerodynamics is therefore likely to affect directly the pilot workload during shipborne operations. To ensure safe maritime operations, each ship/aircraft configuration is tested through expensive and time-consuming campaigns of at-sea trials during which the Ship/Helicopter Operational Limitations (SHOL) are defined for a range of wind strength and direction [9].

Human-in-the-loop flight simulations are an attractive way of extending shipborne operations for dynamic interface testings without the cost and hazard of at-sea campaigns. Such real-time simulations rely on approximate models for computing the aircraft behaviour. Flight mechanics models of various levels of fidelity are used in conjunction with a set of look-up tables to include the aerodynamic effects. For shipborne operations, the ship wake can be steady or unsteady and is most of the time generated using simplified methods. Offline simulations are also considered, using sets of models for the aircraft flight mechanics, pilot controls and disturbances [6]. The notion of coupling is important in the context of ship/helicopter operations: uncoupled simulations assume no effect of the ship wake on the rotor, one-way coupled calculations refer to simulations that account only for the effect of the ship wake onto the rotor while two-way coupled simulations include both ship-on-rotor and rotor-on-ship effects. One-way coupled simulations are typical of flight simulation environments that use steady or unsteady "frozen" ship airwake to generate the look-up tables.

Computational Fluid Dynamics (CFD) methods are efficient tools for the simulation of rotor flows and ship wakes and are already considered as a way to improve flight simulation environments, hence providing pilots with more realistic training tools and ultimately helping broader the range of conditions investigated during at-sea trials to the potentially dangerous flight conditions.

This paper represents a first step in studying the effect of the ship wake on the helicopter flight characteristics. Steady calculations using an actuator disk method were first conducted to assess the coupling effects, followed by unsteady calculations of a fully-articulated Seaking rotor that is used to give more details on the flow characteristics and conclusions in terms of rotor loading.

1.1 Past Numerical Work on Shipborne Rotors

Computational Fluid Dynamics methods have shown promising results for the computation of ship airwakes, despite the complexity of such cases. Key issues are the high Reynolds number of the flow, the wide range of turbulence scales and the large velocity gradients. Some reported studies aimed at implementing CFD-based data into flight simulation systems in order to improve their realism. This is achieved through the use of frozen ship wakes and therefore does not couple the effect of the aircraft itself with the ship wake. A number of ship shapes are used extensively in the literature, amongst them: the Simple Frigate Shape (SFS) and its modification (SFS2), the Canadian Patrol Frigate (CPF) (Figure 1), the Landing Helicopter Assault (LHA), the Type-23 frigate, one of the most popular.

Along with the corresponding wind tunnel experiments (See section 1.2), Syms [29, 30] carried out two sets of numerical simulations at NRC in Canada. The first one uses a pressure-based RANS solver closed by a $k-\epsilon$ turbulence model and a 0.9 million cells structured grid of the CPF model that includes the atmospheric boundary layer in the simulation. Results highlight the importance of the small ship geometry features as well as the limitations of steady-state computations. The second one used the SFS2 ship shape and the Lattice-Boltzmann flow solver PowerFlow. Simulations were unsteady and both RMS and mean values show good agreement with the wind tunnel data.

Numerical simulations of ship airwakes have been conducted at the University of Liverpool using the commercial CFD code Fluent and the SFS2 frigate geometry [7, 21, 22]. The results obtained were compared with experimental data from NRC Canada and exported into look-up tables for utilisation in the university's flight simulator. The first results [21,22] conclude that the use of steady airwakes lead to a very low pilot workload during the simulation. After implementing a set of unsteady airwakes [7], the flight simulation was found to be much more realistic, but with levels of workload sometimes more prononced than expected.

Several studies applied LES-based methods to the computation of ship airwakes, showing great improvements in predicting the flow characteristics, although at a much greater computational cost and despite the use of grids that are not up to the required resolution for LES/DES calculations.

Polsky [18] used the Monotone Integrated Large Eddy Simulation (MILES) method on a 4 million cells grid for the LHA. Results conclude on the necessity of using unsteady simulations regarding the level of instabilities in the flow, and on the dramatic changes of flow topology with the wind direction. It also demonstrates that the flow is Re-independent, as sharp edges lead to fixed flow separation points. The results obtained are representative of a large range of wind velocities and direct velocity rescaling is possible.

Forrest and Owen [5] used Detached Eddy Simulation (DES) and the commercial solver Fluent to simulate the flow over the SFS2 model and the Type-23 frigate. Comparisons with wind tunnel and full scale data show good agreement for mean flow properties in most cases. The frequency and levels of turbulence in the flow are comparable to NRC wind tunnel data.

Thornber *et al.* [32] employed Implicit LES (no explicit sub-grid model) to simulate the airwake of two frigate models (Type-23 and Wave Class AO). The grids had 8 million points and used a block-structured topology. A mean atmospheric

boundary layer was included in the simulation. Results were compared with full-scale measurements and wind tunnel data and show good agreement, especially with full-scale measurements.

As mentioned before, in the context of ship/rotor interaction the coupling is important and the ship airwake alone may have insufficient information to predict the helicopter behaviour. Two-way coupled simulations of the Ship/Helicopter Dynamic Interface (DI) are much more challenging as they involve a wide range of flow conditions: low-speed incompressible and high-speed compressible flows, steady and unsteady behaviours, complex geometries [17]. For these reasons, simplifications are often made when attempting such computations. Polsky conducted MILES simulations for different scenarios [17, 19]: V-22 and JSF in hover near the LHA flight deck, static F-14 in front of a jet blast deflector, F-18 following a prescribed landing path above an aircraft carrier deck and H60 rotor at different positions above a DDG frigate landing spot. Grid sizes ranged from 10 to 29 million cells. An actuator disk method was used to model rotors and jet flows but articulated blades and the addition of a flight mechanics model were considered.

Alpman *et al.* [1] and Bridges *et al.* [3] conducted computations of the Ship/Helicopter dynamic interface, including flight mechanics and pilot models, distinguishing and comparing the 3 types of coupling. Although the method uses simplified geometries (hangar, simple LHA) and computational methods (Blade Element Model), the results permit to highlight the importance of the coupling on the estimated pilot behaviour.

1.2 Experimental Work

Experimental work has been carried out with the objective of further understanding the effect of the ship airwake during shipborne operations.

Sets of wind tunnel experiments using the SFS, SFS2 and CPF geometries have been conducted at NRC in Canada. Pressure and velocity measurements on the SFS and SFS2 models were used extensively for CFD validation purposes [5, 12, 21, 22, 30]. Experiments on the CPF also include a rotor [38], fuselage [14] and fuselage with rotor cases [13]. The loads on the rotor and fuselage for different wind conditions permit to relate to a corresponding pilot workload and such experiments are believed to be an efficient way to compare the effect of the ship/aircraft configuration or different ship geometries on the Ship/Helicopter Operational Limitations.

Another wind tunnel investigation of the ship/rotor interaction was conducted at the Old Dominion University of Virginia using the SFS geometry and a scaled four-bladed propeller [15, 27]. Results were used to assess the effect of the coupling between ship and rotor wakes but is also expected to serve as validation data for CFD.

Iboshi *et al.* investigated the effect of ground and vertical surfaces on a hovering rotor forces and moments as function of different design parameters. Results in terms of rotor thrust, torque, vibratory loads and blades flapping are discussed for different values of $\frac{C_t}{\sigma}$, wall positions, rotor height above ground. Experiments with ground plane and one wall on each side show an increase in torque coefficient with the proximity of the ground and walls height. The flapping amplitude was also studied and showed little variation with height above ground, unless the two walls are placed very close to the rotor, which lead to a much higher flapping amplitude.

The work being conducted by the US Naval Academy in Annapolis used a patrol ship assimilated to a frigate to perform in-situ velocity measurements, making use of a small scale piloted helicopter model to measure far-wake characteristics [25, 26]. Preliminary CFD calculations were used to anticipate on the measurements campaign, helping building the experimental methodology. Wind tunnel experiments on a 4% scale model have also been conducted with a wind velocity of 91m/s to match Reynolds numbers representative of the full-scale ship. The velocity was measured using a 18-hole probe and results compare acceptably with CFD data and at-sea measurements.

For more information on SHOL definition and at-sea campaigns, the reader can refer to the publications by Hoencamp *et al.* in the Netherlands on the Lynx and NH-90 flight testings [8, 9].

1.3 Objectives of the Current Work

The first objective of this paper is to assess the importance of using two-way coupled simulations for the study of Ship/Helicopter operations. Steady-state CFD computations were performed using an actuator disk method to account for the effect of the rotor, which was evaluated for a variety of rotor positions and thrust coefficients.

The superposition method permits to predict a flowfield by adding two separately computed flows. This method is decoupled as it does not account for the effect of each flowfield onto the other. The position of the rotor corresponding to a "station-keeping" maneuver just before touch-down (1 rotor radius above the deck) is chosen and results of this two-way coupled simulation are compared with the result of the direct superposition of the isolated ship and rotor wakes. Coupled simulations are repeated for different rotor locations to study the effect of the aircraft position on the wake.

Secondly, unsteady simulations were performed to overcome the limitations of steady-state simulations. A five-bladed Sea King rotor is simulated in isolated forward flight as well as in the same "station-keeping" condition above the CPF flight deck and the superposition results are compared with results of the isolated and fully-coupled cases.

2 NUMERICAL METHODS

2.1 CFD Solver

The HMB code of Liverpool was used for solving the flow around the different ship and rotor geometries. HMB is a Navier-Stokes solver employing multi-block structured grids. For rotor flows, a typical multi-block topology used in the University of Liverpool is described in Steijl *et al.* [28]. A C-mesh is used around the blade and this is included in a larger H structure which fills up the rest of the computational domain. For parallel computation, blocks are shared amongst processors and communicate using a message-passing paradigme.

HMB solves the Navier-Stokes equations in integral form using the Arbitrary Lagrangian Eulerian (ALE) formulation for time-dependent domains with moving boundaries:

$$\frac{d}{dt}\int_{V(t)} \vec{\mathbf{w}} dV + \int_{\partial V(t)} \left(\vec{F}_i\left(\vec{\mathbf{w}}\right) - \vec{F}_v\left(\vec{\mathbf{w}}\right)\right)\vec{(}n) dS = \vec{S} \quad (1)$$

where $V(t)$ is the time dependent control volume, $\partial V(t)$ its boundary, $\vec{\mathbf{w}}$ is the vector of conserved variables $[\rho, \rho u, \rho v, \rho w, \rho E]^T$. $\vec{F}_i$ and $\vec{F}_v$ are the inviscid and viscous fluxes, including the effects of the time dependent domain.

The Navier-Stokes equation are discretised using a cell-centred finite volume approach on a multi-block grid, leading to the following equations:

$$\frac{\partial}{\partial t}\left(\mathbf{w}_{i,j,k} V_{i,j,k}\right) = -\mathbf{R}_{i,j,k}\left(\mathbf{w}_{i,j,k}\right) \quad (2)$$

where $\mathbf{w}$ represents the cell variables and $\mathbf{R}$ the residuals. i, j and k are the cell indices and $V_{i,j,k}$ is the cell volume. Osher's [16] upwind scheme is used to discretise the convective terms and MUSCL variable interpolation is used to provide up to third order accuracy. The Van Albada limiter is used to reduce the oscillations near steep gradients. Temporal integration is performed using an implicit dual-time stepping method. The linearised system is solved using the generalised conjugate gradient method with a block incomplete lower-upper (BILU) pre-conditioner [2].

2.2 Actuator Disk Method

Actuator disks permit to account for the effect of the rotor without resolving the flow around the blades. Source terms are added to the momentum and energy equations to impose a jump of pressure across the rotor disk. This models the rotor effects without adding to the computational cost. The size, position and attitude (tilt, roll) of the rotor disk is given by the user, together with the thrust coefficient C_T^{UK} and advance ratio μ:

$$C_T^{UK} = \frac{T}{\frac{1}{2}\rho U_{tip}^2 \pi R^2} \quad (3)$$

$$\mu = \frac{U_\infty}{U_{tip}} \quad (4)$$

For an uniform disk, the source term for the momentum equation is expressed, in dimensionless form:

$$\Delta P^* = \frac{\Delta P}{\rho_\infty U_\infty^2} = \frac{\frac{1}{2} T U_{tip}^2}{\frac{1}{2}\rho_\infty U_\infty^2 A U_{tip}^2} = \frac{1}{2}\frac{C_T^{UK}}{\mu^2} \quad (5)$$

In forward flight, the distribution of loading over the disk is not uniform and a more accurate model is required. Shaidakov [23] gave the tools to estimate the intensity of the source term as function of azimuth:

$$\Delta P^* = P_0 + P_s \sin\Psi + P_{2c}\cos 2\Psi \quad (6)$$

Where the P_0, P_s and P_{2c} coefficients are functions of the radius, advance ratio, rotor tilt and thrust coefficient. The load distribution as function of the radius for the advancing and retreating blades are plotted in figure 2. Unlike a real rotor, the actuator disk method imposes a given distribution of additional momentum across the disk - tuned for forward-flying rotors - regardless of the flow conditions. However, the velocities are impacted by the actuator disk as well as the presence of the ship.

2.3 Trimming Method

The trimming method implemented in HMB permits to determine the rotor collective and cyclic inputs to reach a target thrust coefficient while keeping the roll and pitch moments close to zero. The loads on the rotor are calculated after each full revolution and the values of θ_0, θ_{1s} and θ_{1c} are updated consequently using a pre-defined jacobian matrix. The method is iterative and 5 to 10 revolutions are usually necessary to reach a good convergence.

2.4 Numerical Set-up

The current line of investigation is inspired by the experiments of Zan [38] at NRC Canada: the actuator disks are horizontal (no shaft angle) and the positions reproduce the 8 extremas of the measurements domain, the wind angles are 0 and red 12 degrees, the thrust coefficient is $C_T^{UK} = \frac{T}{\rho A(\omega R)^2} = 0.00734$ and the rotor advance ratio reproduces the experimental case with a 19m/s wind, giving $\mu = 0.118$.

Experiments employed a standalone four-bladed rotor [38] as well as a five-bladed rotor with Sea-King fuselage [13]. Both rotors were horizontal, non-articulated and have high values of solidity. Only the rotor is included in the present work and its geometry as well as trim-state are set to realistic values for a full scale rotor in forward flight.

Table 3 gives the flow conditions used for the wind tunnel experiments and present CFD study compared to estimated full-scale values. For numerical stability and mesh economy, the Reynolds numbers chosen for CFD stand between 1 and 10 million for both the ship and the rotor, which represents a compromise between small-scale and full-scale values.

All results are non-dimensionalized so that $U_\infty = 1$, $P_\infty = \frac{1}{\gamma M^2}$, and $b = 1$ where b is the ship beam, which gives a length scaling of 1:16.4 to obtain the full-scale results in meters.

Ship and rotor wakes are characterized by their high levels of vorticity. The vorticity magnitude as defined equation 7 is used in this paper. Considering the ship wake alone, the non-dimensionalized values of the vorticity magnitude can be rescaled to full scale by multiplying by $\frac{U_\infty}{b}$ where b is the ship beam. This is made possible by the fact that the flow over the ship is largely Re-independant.

$$\Omega_{mag} = \sqrt{\left(\frac{dW}{dy} - \frac{dV}{dz}\right)^2 + \left(\frac{dU}{dy} - \frac{dW}{dx}\right)^2 + \left(\frac{dV}{dx} - \frac{dU}{dy}\right)^2} \quad (7)$$

where all quantities are dimensionless. Most of the results are plotted for a dimensionless vorticity magnitude of $\Omega_{mag} = 2$, which corresponds to $2.5s^{-1}$, i.e. 0.4 Hz in a 40 knots wind.

2.4.1 Steady Calculations

The Canadian Patrol Frigate (CPF) geometry was chosen as it represents a good compromise between geometric realism and mesh complexity. The ship baseline grid contains 5.8 million cells and was refined in the vicinity of the ship, resulting in 15.6 million cells. The isolated actuator disk was ran in pure forward flight (no ground effect) using a 1.4 million cells grid.

Figure 3 shows the baseline and refined versions of the grid. The sea and ship are considered as walls, a coarser background is used and the actuator disk in centered position is shown in the figure 3b.

Steady-state calculations were performed using the CPF and an actuator-disk method for modelling the effect of the rotor. Twenty calculations are performed: 1 baseline isolated ship, 1 baseline actuator disk and 8 different positions of the actuator disk are examined for 2 different wind angles: 0 and red 12 degrees. For each case, the actuator disk is in "station-keeping" flight, i.e. steady with respect to the ship.

2.4.2 Unsteady CFD Calculations

URANS calculations were performed using a five-bladed Sea-King rotor. The modified ship grid and rotor grid sizes were 7.6 and 14 million cells respectively (Figure 4).

The rotor grid is a drum embedded in the ship grid using three sliding planes to allow rotation. Similarly, the ship grid is also embedded in a background grid via the use of sliding planes (Figure 5). The rotor was resolved using 720 time steps per revolution.

3 DES AND URANS COMPARISON

One characteristic of bodies such as ships is the presence of unsteady structures in the wake. The frequency of these structures is usually low - below 1Hz - and will impact directly the helicopter aerodynamics and pilot workload when operating in the vicinity of a ship. The large difference in frequency between the rotor aerodynamics and the wake means that coupled calculations require a large number of rotor revolutions to cover one period of the ship wake.

Figures 6 and 7 show instantaneous snapshots of the flow vorticity using DES and URANS methods. The two results show structures of similar size and intensity over the deck. Figure 8 shows the time-varying value of the streamwise velocity for a point centered over the deck at the height of the hangar roof and also shows similar values of unsteadiness. This validates the use of URANS model for ship flows as little improvement is seen via the use of DES.

Figures 9 and 10 show the flow topology obtained using time-averaged URANS and DES calculations. The flow topology is similar in both cases and so is the downwash induced by the presence of the ship in the vicinity of the hangar.

4 ACTUATOR DISK RESULTS

4.1 Coupling Effect

A common method for simulating the Dynamic Interface is to use a simple rotor method (Blade Element Model) and add the velocities from a steady or unsteady "frozen" ship wake. This wake is computed separately, hence neglecting the effect of the rotor on the wake.

The case of a rotor in "station-keeping" maneuver at one rotor radius above the deck (just before touchdown) is chosen and each figure shows the 4 possible configurations: isolated ship, isolated actuator disk in forward flight, superposition of the two cases and coupled simulation. As previously, two wind angles are considered: 0 and red 12 degrees.

The superposition was performed by combining the flowfield variables point by point. The non-dimensional velocities ($\underline{u} = [u, v, w]^T$) are written as $u = U + \tilde{u}$ where U is the mean value and $\tilde{u}$ is the perturbation. Since the mean value is identical for both case:

$$\underline{u}^{Superposition} = \underline{U} + \underline{\tilde{u}}^{CPF} + \underline{\tilde{u}}^{AD} \tag{8}$$

With $\underline{U} = [1, 0, 0]^T$ for the 0 degrees wind angle case, and $\underline{U} = [\cos(12), \sin(12), 0]^T$ for the red 12 degrees wind angle case. The pressure and density are simply averaged locally

$$p^{combination} = \frac{p^{CPF} + p^{AD}}{2} \tag{9}$$

$$\rho^{combination} = \frac{\rho^{CPF} + \rho^{AD}}{2} \tag{10}$$

The vorticity is then recomputed in each cases from the new variables.

Figures 11 and 12 show iso-contours of vorticity with streamlines and maps of the vorticity at the back of the rotor for each of the 4 cases. The main charateristic of the isolated ship wake (a) is the presence of the mixing layer that separates the recirculation zone, made visible by the streamlines behind the hangar, from the rest of the flow that passes over the hangar roof and on the side of the ship, generating two weak contra-rotating vortices in the vicinity of the ship. The baseline rotor (b) shows typical contra-rotating supervortices that are convected downstream with very little weakening. The superposition (c) shows the same flow characteristics as the two previous cases, with no visible coupling effects. However, the coupled case clearly shows an interaction between rotor and ship wakes: in particular, the velocity seen by the actuator disk is greatly reduced compared to the isolated case. The supervortices are pushed further downward, where the flow is effectively blocked by the presence of the hangar, and pair with vortical structures from the ship wake downstream. While the isolated rotor shows well-confined vortical structures, the coupled case shows lower levels of vorticity, with a larger spatial extent. The streamlines also suggest a recirculation zone behing the hangar door reinforced by the effect of the rotor blowing over the deck.

Results at 12 degrees (Figures 13 and 14) show a significantly different flowfield but similar conclusions: the superposition case shows no differences with the rotor and ship taken separately, the interactional effects are clearly visible and the large vortex shed from the windward edge of the hangar pairs with the rotor wake as the two vortices are co-rotatings. The rotor vortex on the leeward side remains in the zone of low velocity behind the hangar and is convected slower downstream. The streamlines for the coupled case again suggest a reinforced recirculation zone, which is not

visible on the superposition case. The vorticity map for the coupled simulation show a clear dissymmetry between the two sides of the rotor: the aircraft operating behind the ship is likely to experience important variations of loading and therefore increase the pilot worload and reduce power and control margins.

4.2 Effect of the Rotor Thrust

The 12 degrees wind angle is reproduced with 4 times the value of the thrust coefficient, i.e. $C_T^{UK} = 0.02936$. Figure 15 shows the results in terms of vorticity for the isolated ship and shipborne actuator disk at $C_T^{UK} = 0.00734$ and $C_T^{UK} = 0.02936$. The deck creates an effective blockage that can be seen as a "partial ground effect" and forces the wake to expand laterally. As a result, the wake remains closer to the deck, in a zone of low velocity behind the hangar, showing little supervortices, especially on the leeward side.

Although the simulations were steady and used a simplified rotor model, this study of the coupling effect between a rotor and ship wake suggests that the case of a rotor "station-keeping" over the deck before touchdown can not be simulated by superimposing the flowfield obtained for an isolated rotor to the wake of the isolated ship.

The following section aims at estimating the extent of the mutual influence between the ship and rotor wakes.

4.3 Influence of the rotor position

Figure 16 shows the distribution of downwash velocity in the region of the disk for 8 different positions of the actuator disk at 0 degrees WOD angle. Important differences in terms of downwash velocity are found between the inboard and outboard regions of the disk, especially for upwind cases. This suggests an important variation of rotor trim-state as the aircraft maneuvers in this particular region, and therefore a corresponding action of the pilot and an increased workload.

At 12 degrees, (Figure 17) the distribution of velocity is no longer symmetrical and the windward and leeward rotors operate in very different flowfields: upwash with strong vortical structure on the windward side, downwash on the leeward side

The upwind rotor, on the leeward side of the ship in "station-keeping" at 9 meters can be seen as a worst-case scenario as the rotor operates in a strong downwash, therefore reducing the control and power margins.

The effect of the ship wake is stronger at 9 meters above the deck but shows a significant effect even at 15 meters, suggesting that the interactional effect between the ship and the helicopter extends outside the immediate vicinity of the ship.

To compare the relative strength of the rotor and ship wakes, maps of the vorticity are plotted at the back of each upstream actuator disk, demonstrating the impact of the rotor on the ship wake (Figure 18). The baseline cases are given for comparison and correspond to the ship airwake with no actuator disk.

Overall, at the chosen thrust coefficient, ship and rotor wakes show similar levels of vorticity. At 0 degrees (left-hand-side figures), the blowing effect of the actuator disk causes the ship wake to lose its symmetry and cases at 9 meters above the deck clearly show interaction between the two wakes that is less sensible at 15 meters. However, and for every case, the corresponding rotor and ship vortices are contra-rotative, preventing them from pairing and therefore limiting the interactional effects: in snapshot (c) and (d), the rotor supervortex on the right-hand side of the disk rotates in the counter-clockwise direction while the left-hand side of the ship wake rotates clockwise.

As mentioned before, the case of a rotor in upwind position on the leeward side of the ship is believed to be the most demanding for the aircraft as the rotor is directly in the vicinity of the ship, in a region of strong downwash that reduces significantly the power and control margins of the aircraft. This situation was chosen to assess the effect of the rotor thrust: 3 different values of thrust are used (1, 2 and 4 times the thrust used for previous cases) at $C_T^{UK} = 0.00734$, 0.01468 and 0.02936. Figure 19 shows the results in terms of vorticity magnitude. The vorticity clearly increases with the thrust as well as the interactional effect with the ship wake. However, the influence remains limited to a region of the flow close to the rotor and does not extend enough upstream to change significantly the topology of the ship wake itself.

The actuator disk method is an efficient tool for capturing the main flow characteristics of coupled Ship/Rotor simulations. This study also shows that two-way coupled calculations are necessary as they capture coupling effects that are not represented by combination of the ship and rotor wake. However, the use of steady calculations and a simplified model of actuator disk that has been tuned to be representative of forward-flying rotors may not be satisfactory for high fidelity simulations. To overcome the limitations of the actuator disk model and predict accurate helicopter loads, coupled simulations with fully-articulated rotor blades and helicopter fuselage are necessary.

5 SHIPBORNE SEA-KING ROTOR

This section reproduces the case of a rotor in "station-keeping" at 1 rotor radius above the deck (i.e. just before touchdown) using an unsteady simulation that includes a full Sea-King rotor with five articulated blades.

5.1 Rotor Trimming

First, the isolated rotor is trimmed in terms of blade collective and cyclic using the previous target thrust coefficient $C_T^{UK} = 0.00734$ and zero moment in pitching and rolling (figure 20). The rotor assembly is assumed to be completely rigid and therefore no blade flapping harmonics are applied. The isolated rotor ran for 6 revolutions to reach a converged state then was trimmed over 4 additional revolutions. The operation is repeated for the shipborne rotor: after convergence using the previous trim state (10th revolution), only 2 more revolutions were necessary to adjust the trim state to the new flow conditions. The final trim state of both rotors is presented table 4. The shipborne rotor is also re-trimmed to a new target thrust coefficient of $C_T^{UK} = 0.01468$, corresponding to exactly twice the previous value, as for the actuator disk case. This is refered to as "high-thrust" case in the following.

The values of collective and cyclic pitch θ_0, θ_{1c}, θ_{1s} correspond to the amplitude of the mean, cosine and sine com-

ponents of a negative Fourier decomposition:

$$\theta = \theta_0 - \theta_{1c} \cos \Psi - \theta_{1s} \sin \Psi \quad (11)$$

5.2 Shipborne Rotor Flow Topology

Figure 21 shows iso-contours and maps of vorticity for the ship alone, rotor alone, ship and rotor combined using superposition method and coupled calculation with a red 12 degrees wind. The supervortices on each side of the isolated rotor are clearly visible, as well as the signature of the blade tip vortices in the rotor wake. The superposition method shows similar results as with the actuator disk study: the flow topology after superposition shows no additional effect due to an interaction between the two wakes. In case of a coupled simulation, the super-vortices seem to be altered by the ship wake and do not live long enough to be convected with the ship wake.

Maps of vorticity show a slice of the rotor wake with values of vorticity and a wake topology similar to the actuator disk cases. The rotor wake appears to be significantly stronger in terms of vorticity than the ship wake for this rotor location and therefore the effect of the rotor onto the ship wake is expected to be strong, ruling out the use of the superposition method.

The high-thrust case presented in figure 21(e) shows an increase of vorticity in the wake. The wake is also pushed further down underneath the rotor but the flow topology remains similar.

Figure 22 shows a comparison of the flow topology with an actuator disk and a fully-articulated rotor at the same position over the deck. Differences are found in terms of flow topology, especially in the recirculation zone behind the hangar that is located further downstream in the rotor calculation. The isolated rotor flow is added for comparison and shows significant differences with the shipborne rotor case in terms of downwash intensity. The effect of the blade tip vortices is also visible on both isolated and shipborne rotors. The downwash intensity is also much stronger in the high-thrust case, the wake extends further and the ground effect is expected to play a more important role in this case.

Figures 23 and 24 show maps of downwash velocity through the rotor disk for an isolated rotor, shipborne actuator disk and 4 different azimuthal positions of the shipborne rotor. The ship hull is outlined when the ship is present in the simulation.

The difference in inflow distribution due to the ship is visible and will impact directly the rotor capabilities by changing the angle of attack seen by the blades (See 5.3). The actuator disk method shows good agreement in terms of downwash distribution across the disk.

The surface flow topology is presented figure 25 using streamlines and pressure contours on the deck. Firstly, a recirculation zone is located behind the hangar and reattaches in the middle of the deck, showing a rise of pressure on the deck. This pressure rise is more important and extends further with the presence of the rotor blowing over the deck. The flow presents some small features such as the vortex starting from the port side of the deck behind the hangar that disappears in the presence of the rotor.

5.3 Rotor Loading

Actuator disk methods assume a fixed rotor loading, which has been tuned for forward-flying rotors. Rotor calculations permit to determine the actual rotor loading for any flight conditions, it is therefore possible to compare isolated and shipborne rotor loadings.

Figures 26, 27 and 28 show the distribution of loading for an isolated rotor in trimmed forward flight, the same rotor, under the same conditions, behind the Canadian Patrol Frigate and after a second trimming in the ship wake. There are significant differences in terms of thrust on the front and starboard side of the disk, where the downwash behind the hangar tends to decrease the angle of attack of the blades. On the port side, the upwash caused by the side-wind deviated by the hull maintains a high loading. This is consistent with pilot feedbacks that indicate a roll-off behaviour of the aircraft when entering the region of the flow directly behind the hangar [39]. The second trimming imposes a higher collective to balance the loss of thrust and changed both the sine and cosine terms to restore the rotor balance in terms of pitch and roll moments. The fourth element of each figure corresponds to the high-thrust case. The observed distributions of normal force, pitching moment and torque coefficients are similar, although with less variations around the azimuth.

Results obtained for the shipborne rotor show a diminution of thrust of about 18% compared to the isolated rotor in forward flight at the same trim state. This is consistent with the observations of Zan [38] that showed a reduction of about 10% for the headwind case and a further diminution when the rotor was located in the leeward side of the ship with a 12 degrees wind angle.

6 Conclusions and Future Work

Numerical simulation of shipborne rotors have been conducted using the simplified actuator disk method and a fully articulated Sea-King rotor. Results show similar levels of wake intensity between the rotor and ship wake and an important dependance of the flowfield to wind angle as well as rotor position. In cases where the rotor is located directly in the vicinity of the ship, the two wakes encounter, which leads to significant coupling effects. URANS and DES models show similar topology and levels of vorticity for the isolated ship, validating the URANS model for the simulation of ship flows. Further calculations were performed using the models, in a steady or unsteady fashion, but using coarser grids that showed mainly the steady flow characteristics and little unsteadiness.

Some flight simulations use direct superposition of the rotor and ship wake, hence neglecting the effect of the rotor on the wake. To assess the validity of such method, the coupled wake was compared with the result of a direct superposition. The superposition did not model the interactional effect of the two wakes that lead to the formation of larger vortices behind the rotor.

The results obtained showed that steady simulations with an actuator disk model permit to predict reasonably well the main flow characteristics. The limitations of the actuator disk model can be overcome by using full rotor blades and unsteady calculations, albeit at a greater computational cost.

The rotor loading can then be calculated and the trim state tuned to achieve steady flight. The results showed significant differences in rotor loading for the same flight conditions between the rotor in isolated forward-flight and in the vicinity of the ship. The leeward side of the deck sees a downwash from the hangar rooftop to the deck which reduces the loading while the windward side benefits from the upwash due to the wind impinging the hull. The resulting changes in forces and moments have to be balanced by an action of the pilot and contribute to the total workload. The global effect of the ship wake is a diminution of almost 20% in rotor thrust and this is consistent with the published experimental data [38].

To enhance the realism of the simulations, a flight mechanics method is being implemented in HMB. The demonstration and validation of this code for the simulation of freely-flying aircraft and the application to the case of a ship landing maneuver is part of the future work.

7 Acknowledgements

The support of this project by AgustaWestland Liverpool Advanced Rotorcraft Center is gratefully acknowledged. The authors would like to thank the N8 High Performance Computing (N8 HPC) centre for the use of CPU time.

References

[1] E. Alpman, L.N. Long, D.O. Bridges, and J.F. Horn. Fully-Coupled Simulations of the Rotorcraft/Ship Dynamic Interface. In *Annual Forum Proceedings - American Helicopter Society*, volume 63, page 1367. American Helicopter Society, inc, 2007.

[2] O. Axelsson. *Iterative Solution Methods*. Cambridge University Press: Cambridge, MA, 1994.

[3] D. O. Bridges, J. F. Horn, E. Alpman, and L. N. Long. Coupled flight dynamics and cfd analysis of pilot workload in ship airwakes. In *Collection of Technical Papers - 2007 AIAA Atmospheric Flight Mechanics Conference*, volume 1, pages 471–489, 2007.

[4] B.T. Cheney and S.J. Zan. Cfd code validation data and flow topology for tccp aer-tp-2 simple frigate shape. *Ottawa, Canada*, 1999.

[5] J.S. Forrest and I. Owen. An investigation of ship airwakes using Detached-Eddy Simulation. *Computers and Fluids*, 39(4):656 – 673, 2010.

[6] R.A. Hess. Simplified technique for modeling piloted rotorcraft operations near ships. *Journal of guidance, control, and dynamics*, 29(6):1339–1349, 2006.

[7] S. J. Hodge, S. J. Zan, D. M. Roper, G. D. Padfield, and I. Owen. Time-accurate ship airwake and unsteady aerodynamic loads modeling for maritime helicopter simulation. *Journal of the American Helicopter Society*, 54(2):0220051–02200516, 2009.

[8] A.a Hoencamp and M.D.b Pavel. Flight test results nh90 nfh helicopter-ship qualification process. volume 3, pages 2177–2188, 2012.

[9] A.a Hoencamp, Th.b Van Holten, and J.V.R.c Prasad. Relevant aspects of helicopter-ship operations. *34th European Rotorcraft Forum 2008, ERF34*, 1:578–588, 2008.

[10] W. Johnson. Wind tunnel measurements and calculations of aerodynamic interactions between tiltrotor aircraft. Technical report, DTIC Document, 2003.

[11] C.H. Kaaria, J.S. Forrest, I. Owen, and G.D. Padfield. Simulated aerodynamic loading of an sh-60b helicopter in a ship's airwake. *35th European Rotorcraft Forum 2009, ERF 2009*, 2:1001–1013, 2009.

[12] S.J. Lawson, F. Dehaeze, and G.N. Barakos. Computational fluid dynamics analysis of ship air wakes using detached-eddy simulation. *Journal of Wind Engineering & Industrial Aerodynamic*, 2011.

[13] R.G. Lee and S.J. Zan. Wind tunnel testing of a helicopter fuselage and rotor in a ship airwake. *Journal of the American Helicopter Society*, 50:326, 2005.

[14] R.G. Lee, S.J. Zan, et al. Unsteady aerodynamic loading on a helicopter fuselage in a ship airwake. *Journal of the American Helicopter Society*, 49:149, 2004.

[15] Y.a. Nacakli and D.b. Landman. Helicopter downwash/frigate airwake interaction flowfield piv surveys in a low speed wind tunnel. *Annual Forum Proceedings - AHS International*, 4:2988–2998, 2011.

[16] S. Osher and S. Chakravarthy. Upwind Schemes and Boundary Conditions with Applications to Euler Equations in General Geometries. *Journal of Computational Physics*, 50:447–481, January–February 1983.

[17] S. Polsky. Progress towards modeling ship/aircraft dynamic interface. In *HPCMP Users Group Conference, 2006*, pages 163–168. IEEE, 2006.

[18] S.A. Polsky. A computational study of unsteady ship airwake. Technical report, DTIC Document, 2003.

[19] S.A. Polsky. Computational analysis for air/ship integration: 1st year report. In *High Performance Computing Modernization Program Users Group Conference (HPCMP-UGC), 2010 DoD*, pages 109–114. IEEE, 2010.

[20] G. Rajagopalan, S. Niazi, AJ Wadcock, GK Yamauchi, and MJ Silva. Experimental and computational study of the interaction between a tandem-rotor helicopter and a ship. In *Annual Forum Proceedings - American Helicopter Society*, volume 61, page 729. American Helicopter Society, inc, 2005.

[21] D.M. Roper, I. Owen, G.D. Padfield, and S.J. Hodge. Integrating CFD and Piloted Simulation to Quantify Ship-Helicopter Operating Limits. *Aeronautical Journal*, 110(1109):419–428, 2006.

[22] D.M.a Roper, I.b Owen, and G.D.c Padfield. Cfd investigation of the helicopter-ship dynamic interface. *Annual Forum Proceedings - AHS International*, 2:1985–2002, 2005.

[23] V.I. Shaidakov. Disk vortex theory of main rotor with constant loading on the disk. *Helicopters Design Aerodynamics*, 381, 1976.

[24] M.J. Silva. Wind tunnel investigation of the aerodynamic interactions between helicopters and tiltrotors in a shipboard environment. Technical report, DTIC Document, 2004.

[25] M. Snyder, H. Kang, and J. Burks. Validation of computational ship air wakes for a naval research vessel. *51st AIAA Aerospace Sciences Meeting including the New Horizons Forum and Aerospace Exposition*.

[26] M.R. Snyder, J.S. Burks, C.J. Brownell, L. Luznik, D.S. Miklosovic, J.H. Golden, M.E. Hartsog, G.E. Lemaster, F.D. Roberson, J.P. Shishkoff, W.P. Stillman, and C.H. Wilkinson. Determination of shipborne helicopter launch and recovery limitations using computational fluid dynamics. *Annual Forum Proceedings - AHS International*, 4:3136–3146, 2010.

[27] D. Stargel and D. Landman. A wind tunnel investigation of ship airwake/rotor downwash coupling using design of experiments methodologies. In *50th AIAA Aerospace Sciences Meeting including the New Horizons Forum and Aerospace Exposition, Nashville, Tennessee*, 2012.

[28] R. Steijl, G. Barakos, and K. Badcock. A Framework for CFD Analysis of Helicopter Rotors in Hover and Forward Flight. *International Journal for Numerical Methods in Fluids*, 51(8):819–847, 2006.

[29] G.F. Syms. Numerical simulation of frigate airwakes. *International Journal of Computational Fluid Dynamics*, 18(2):199–207, 2004.

[30] G.F. Syms. Simulation of simplified-frigate airwakes using a lattice-boltzmann method. *Journal of Wind Engineering and Industrial Aerodynamics*, 96(6-7):1197 – 1206, 2008. 5th International Colloquium on Bluff Body Aerodynamics and Applications.

[31] Dinu A. Tang L. and Polsky S. Reduced-order modeling of rotor-ship interaction. In *50th AIAA Aerospace Sciences Meeting, AIAA 2012-1300, Nashville, Tenessee*, 2012.

[32] B. Thornber, M. Starr, and D. Drikakis. Implicit large eddy simulation of ship airwakes. 2010.

[33] A.J. Wadcock. Piv measurements of the wake of a tandem-rotor helicopter in proximity to a ship. Technical report, DTIC Document, 2004.

[34] NH Wakefield, SJ Newman, and PA Wilson. Cfd predictions of the influence of external airflow on helicopter operations when operating from ship flight decks. In *RTO applied vehicle technology panel symposium*, pages 2–1, 1999.

[35] NH Wakefield, SJ Newman, and PA Wilson. Helicopter flight around a ship's' superstructure. *Proceedings of the Institution of Mechanical Engineers, Part G: Journal of Aerospace Engineering*, 216(1):13, 2002.

[36] G.K. Yamauchi, A.J. Wadcock, and M.R. Derby. Measured aerodynamic interaction of two tiltrotors. In *Annual Forum Proceedings - American Helicopter Society*, volume 59, pages 1720–1731. American Helicopter Society, inc, 2003.

[37] S.J. Zan. Surface flow topology for a simple frigate shape. *Canadian Aeronautics and Space Journal*, 47(1):33–43, 2001.

[38] S.J. Zan. Experimental Determination of Rotor Thrust in a Ship Airwake. *Journal of the American Helicopter Society*, 47, 2002.

[39] S.J. Zan. On Aerodynamic Modeling and Simulation of the Dynamic Interface. *Proceedings of the Institution of Mechanical Engineers, Part G: Journal of Aerospace Engineering*, 219(5):393–410, 2005.

[40] S.J. Zan, G.F. Syms, and B.T. Cheney. Analysis of patrol frigate air wakes. In *RTO applied vehicle technology panel symposium*, pages 7–1, 1999.

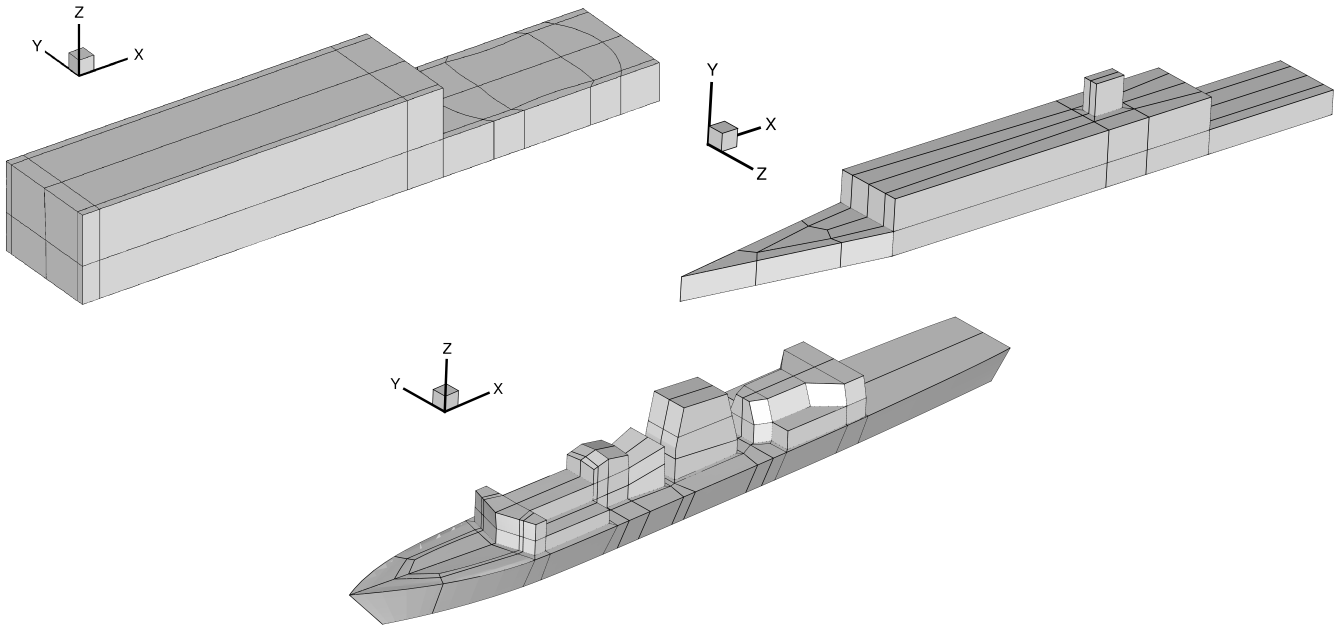

Figure 1: Geometries of the Simple Frigate Shape models and the Canadian Patrol Frigate used for the present work.

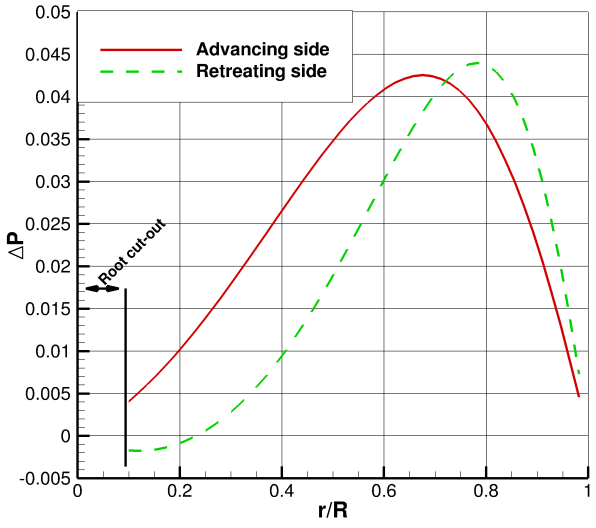

Figure 2: Distribution of loading as function of radius for advancing ($\Psi = \frac{\pi}{2}$) and retreating ($\Psi = \frac{3\pi}{2}$) blades.

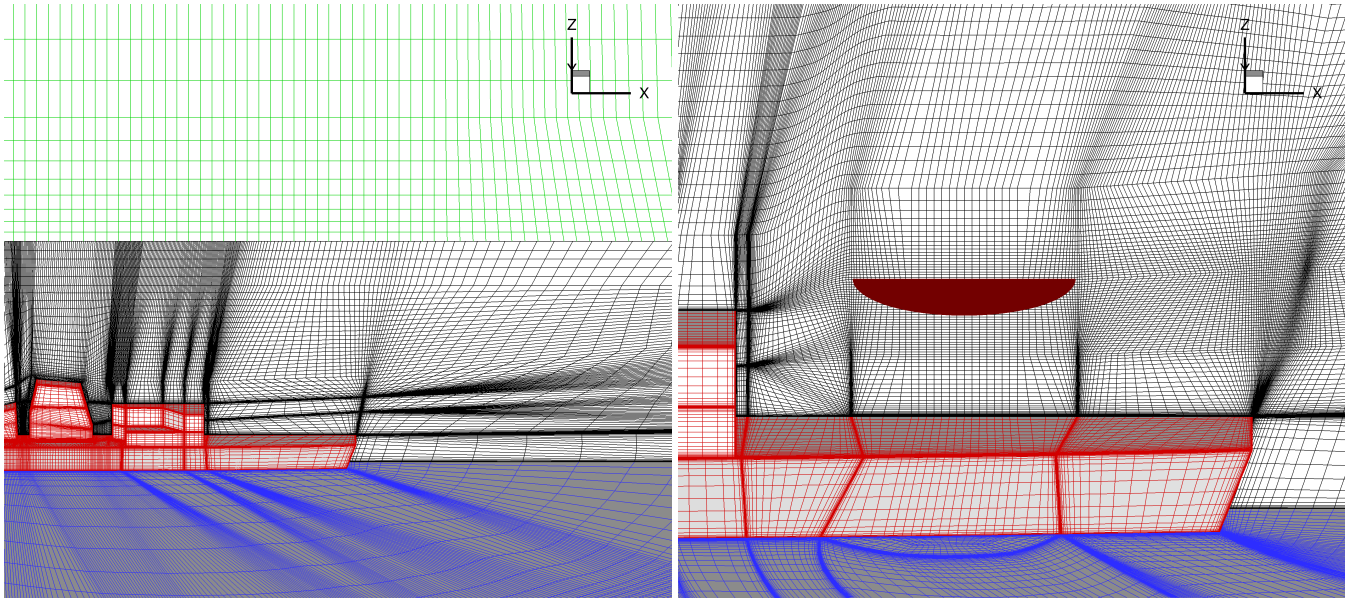

(a) (b)

Figure 3: Views of the grids used for actuator disk simulations. (a) overview and (b) close view on the refined grid showing the position of the actuator disk.

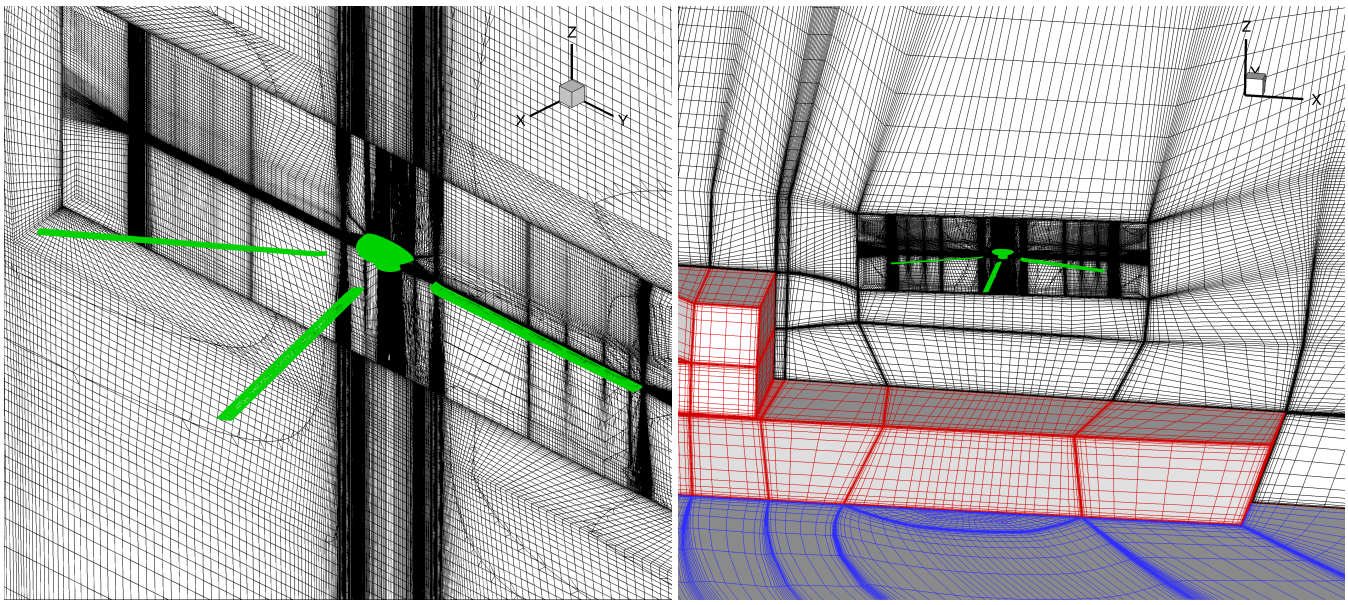

(a) (b)

Figure 4: Views of the grids used for rotor calculations. The rotor grid is identical for both cases and consists of a drum that is embedded in a background grid (a) for isolated forward-flying rotor calculations, or the ship grid (b) for shipborne simulations. Sliding planes are used to interface the two grids.

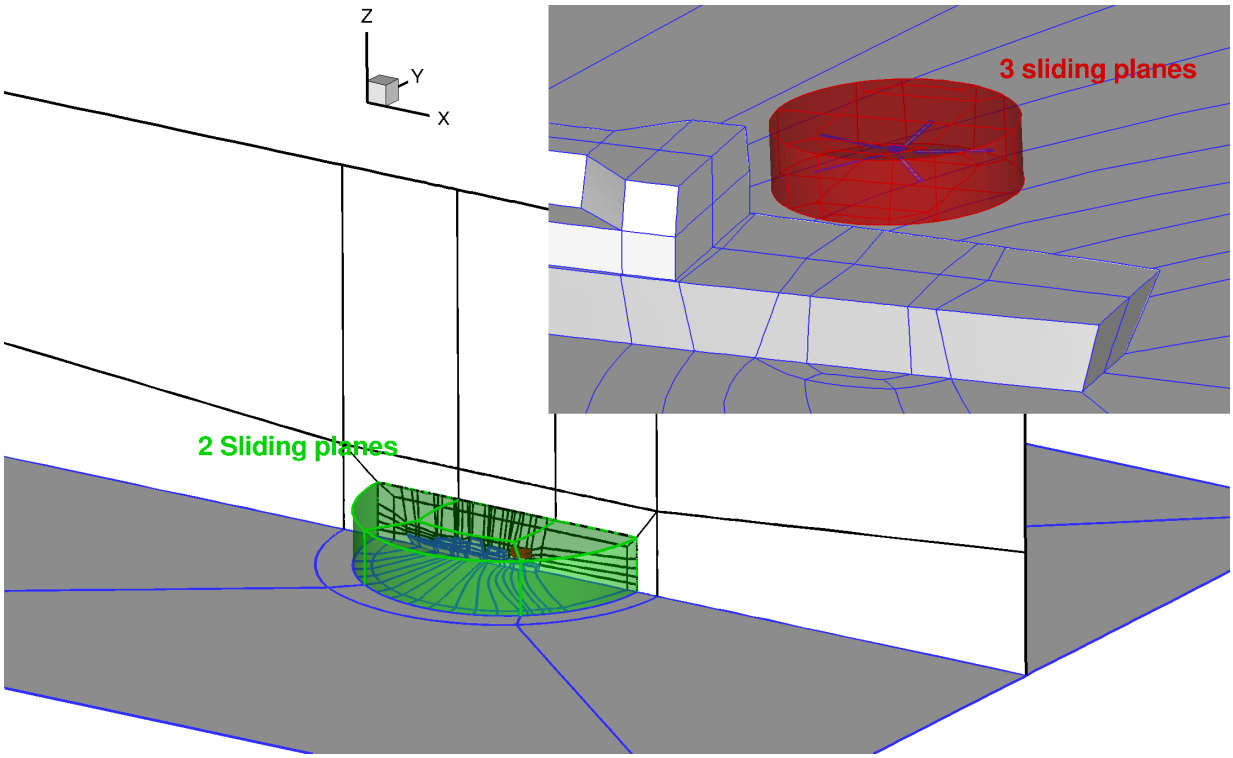

Figure 5: Sliding plane interfaces for the shipborne rotor grid. The rotor drum is embedded in the ship grid using three sliding planes (in red) and the ship grid itself is included in a background grid via two sliding planes (in green).

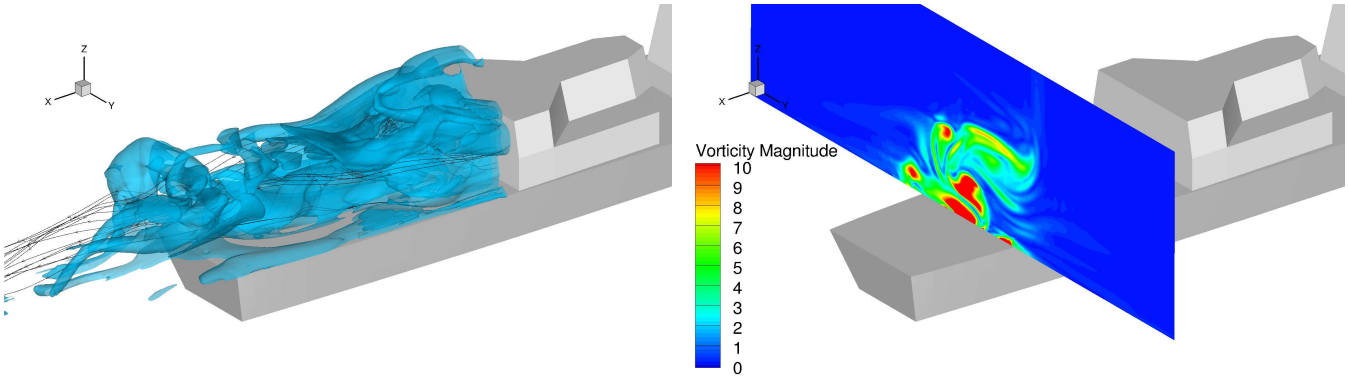

(a) (b)

Figure 6: Instantaneous (a) contours of iso-vorticity $\Omega_{mag} = 6$ and streamlines and (b) map of vorticity for isolated ship using Detached eddy Simulation, at 12 degrees WOD

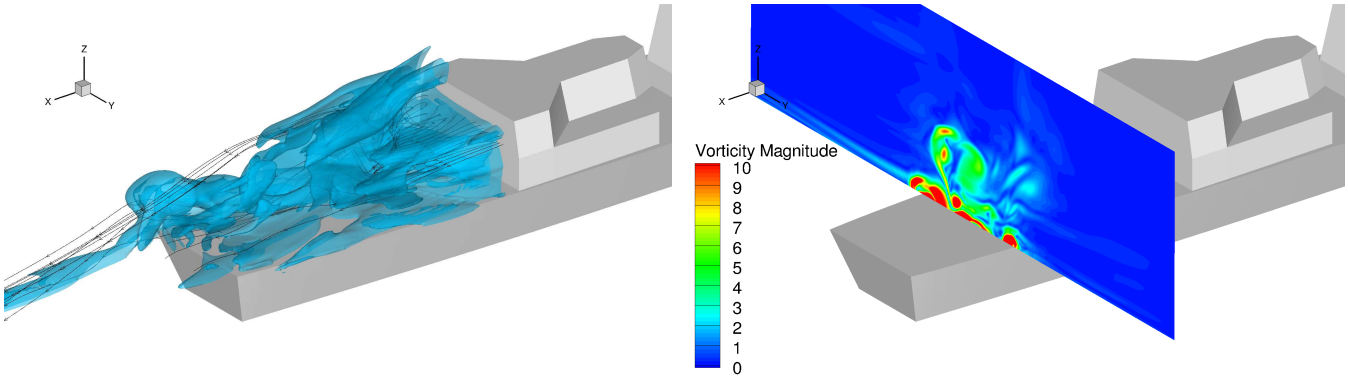

(a) (b)

Figure 7: Instantaneous (a) contours of iso-vorticity $\Omega_{mag} = 6$ and streamlines and (b) map of vorticity for isolated ship using Unsteady RANS calculation, at 12 degrees WOD

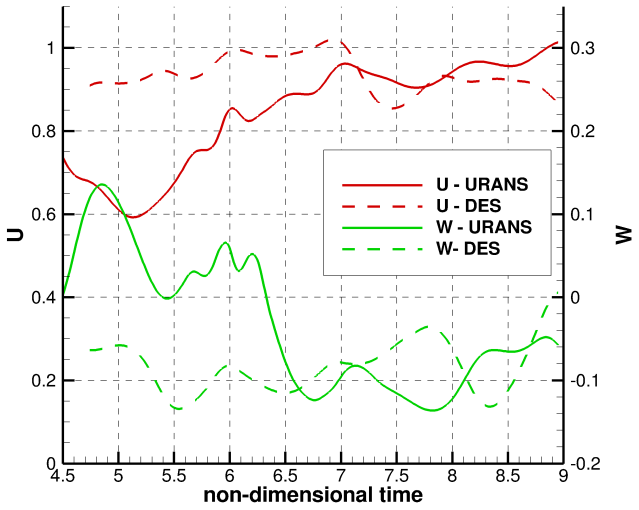

Figure 8: Non-dimensional velocities as function of time at a point centered over the deck using URANS and DES models.

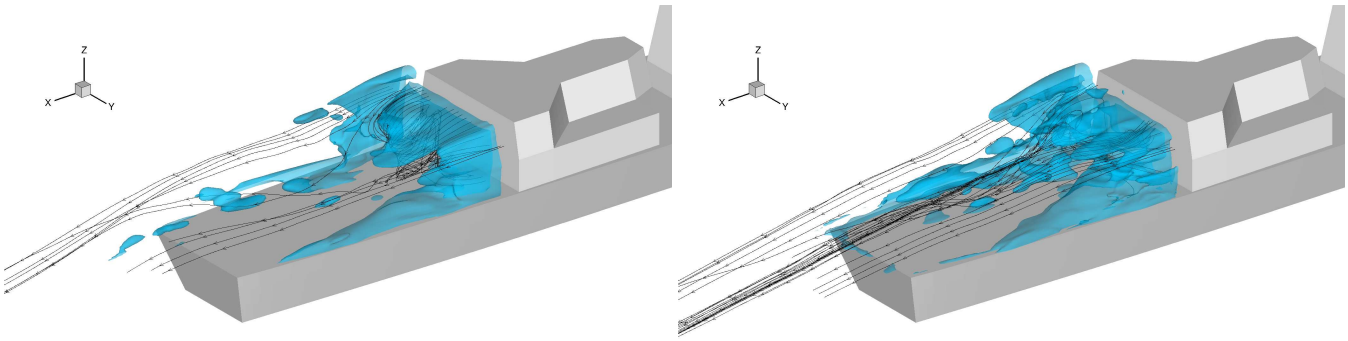

(a) URANS (b) DES

Figure 9: Comparison between URANS and time-averaged DES flow topologies over the CPF deck.

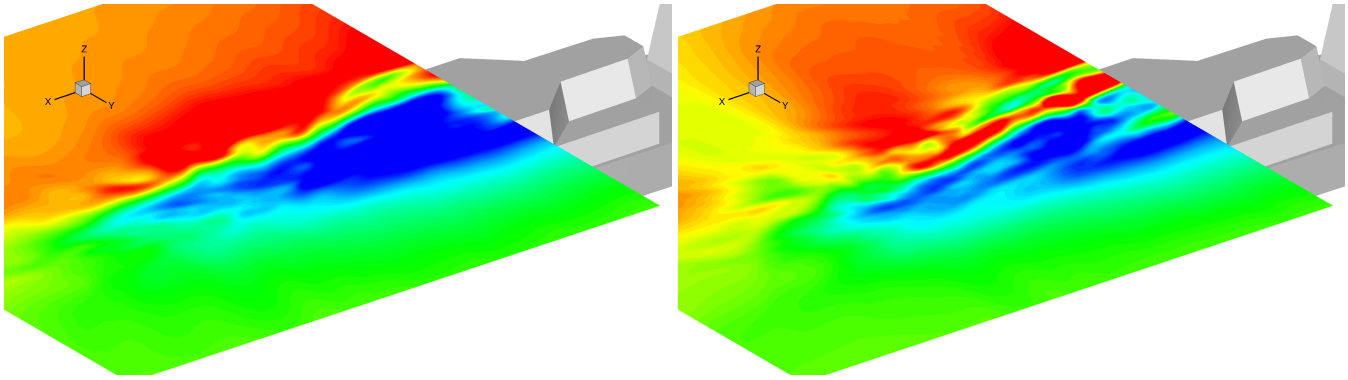

(a) URANS (b) DES

Figure 10: Comparison between URANS and time-averaged DES downwash distribution over the CPF deck.

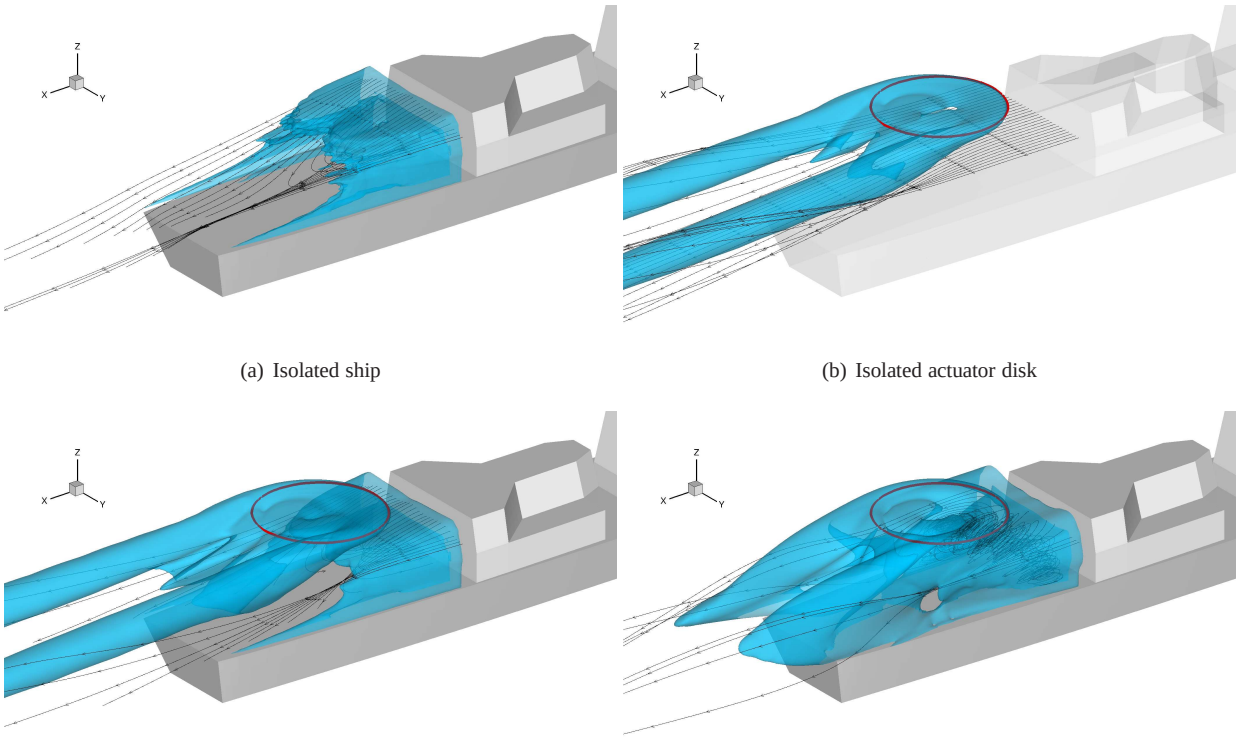

(a) Isolated ship

(b) Isolated actuator disk

(c) Superposition actuator disk and ship wakes

(d) Actuator disk on ship

Figure 11: Iso-vorticity $\Omega_{mag} = 2$ of isolated ship, isolated actuator disk, shipborne actuator disk and superposition of isolated AD and ship at 0 degrees WOD, $C_T = 0.00734$

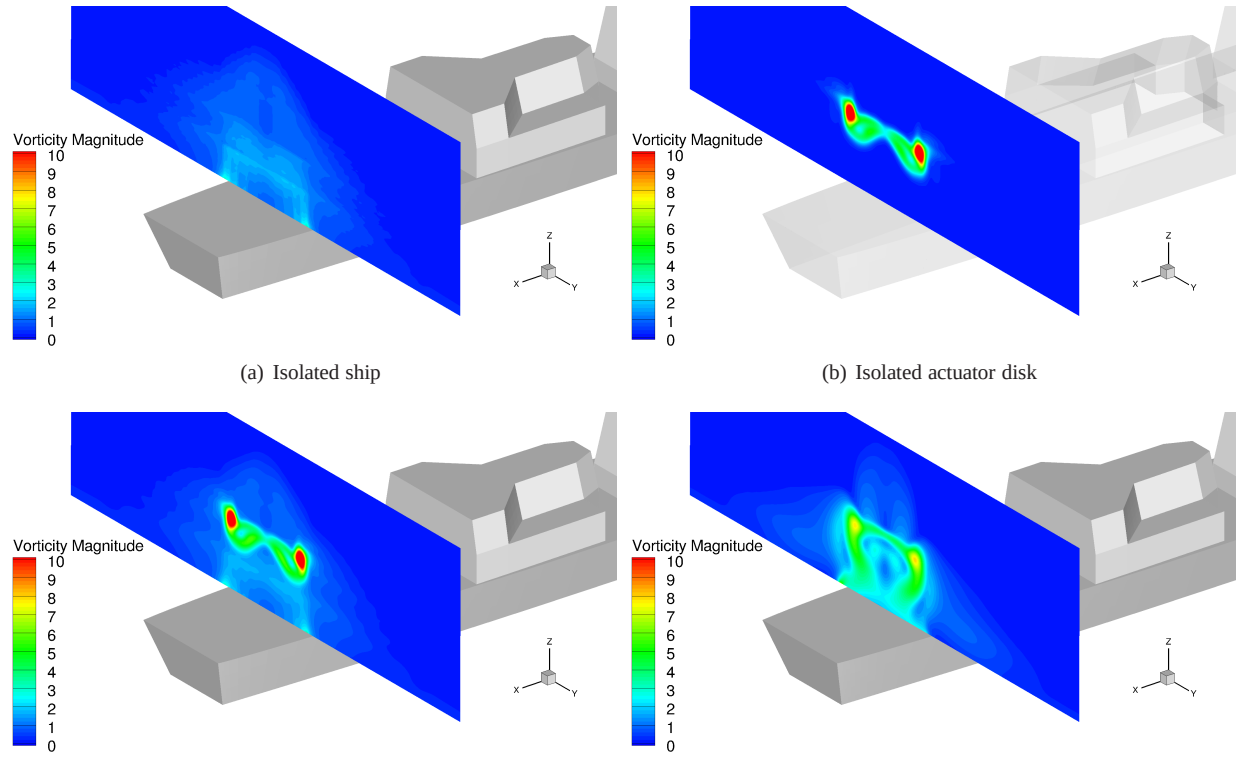

(a) Isolated ship

(b) Isolated actuator disk

(c) Superposition actuator disk and ship wakes

(d) Actuator disk on ship

Figure 12: Maps of vorticity at back of the disk of isolated ship, isolated actuator disk, shipborne actuator disk and superposition of isolated AD and ship at 0 degrees WOD, $C_T = 0.00734$

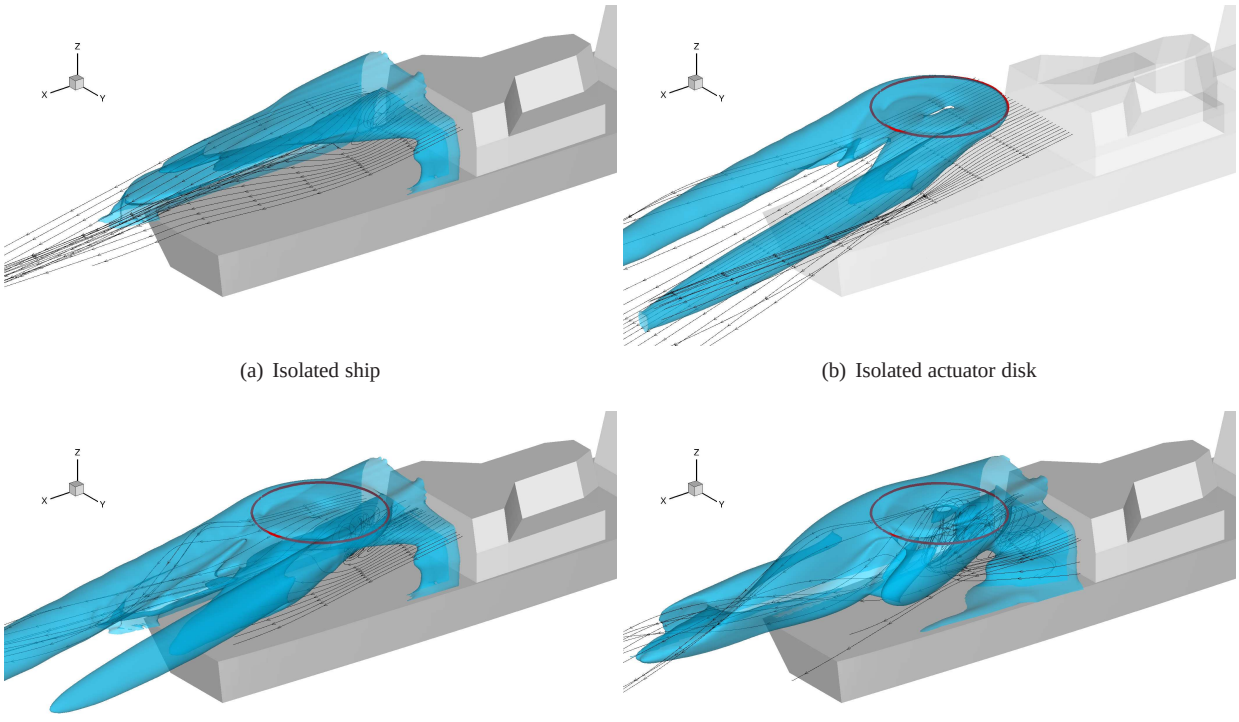

(a) Isolated ship

(b) Isolated actuator disk

(c) Superposition actuator disk and ship wakes

(d) Actuator disk on ship

Figure 13: Iso-vorticity $\Omega_{mag} = 2$ of isolated ship, isolated actuator disk, shipborne actuator disk and superposition of isolated AD and ship at 12 degrees WOD, $C_T = 0.00734$

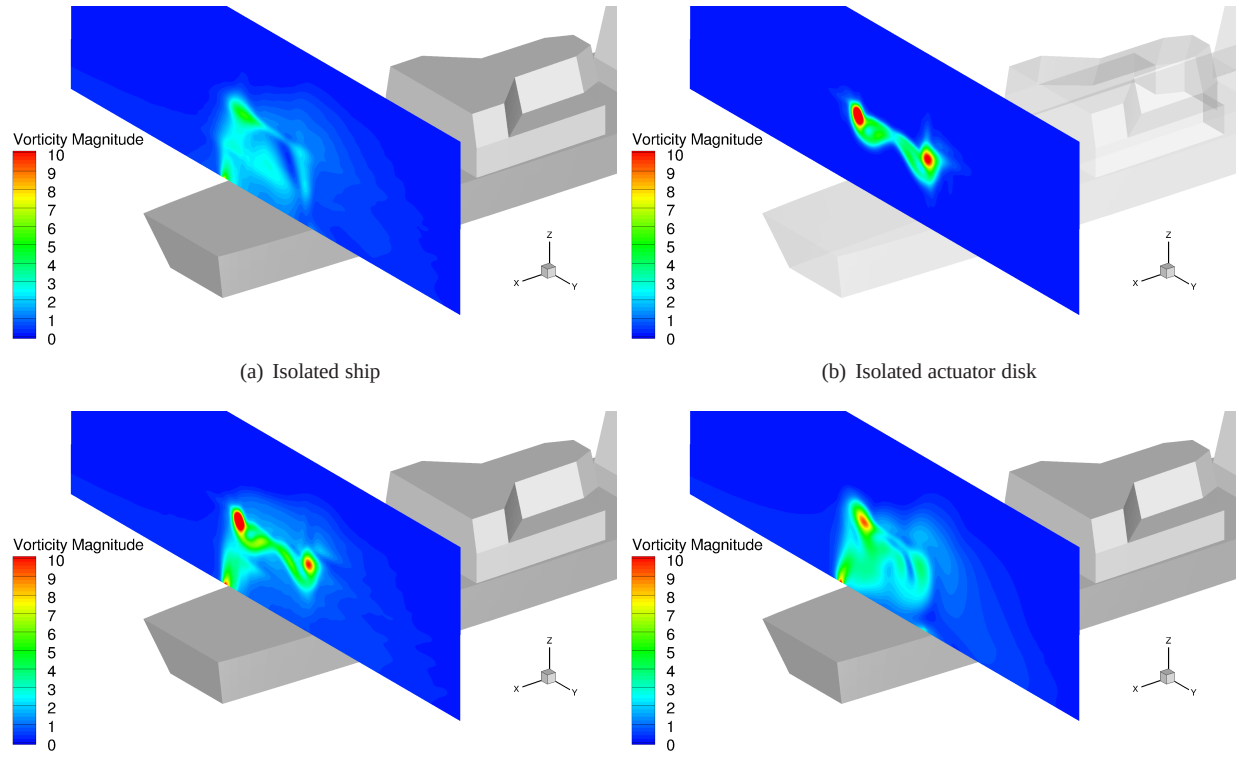

(a) Isolated ship

(b) Isolated actuator disk

(c) Superposition actuator disk and ship wakes

(d) Actuator disk on ship

Figure 14: Maps of vorticity at back of the disk of isolated ship, isolated actuator disk, shipborne actuator disk and superposition of isolated AD and ship at 12 degrees WOD, $C_T^{UK} = 0.00734$

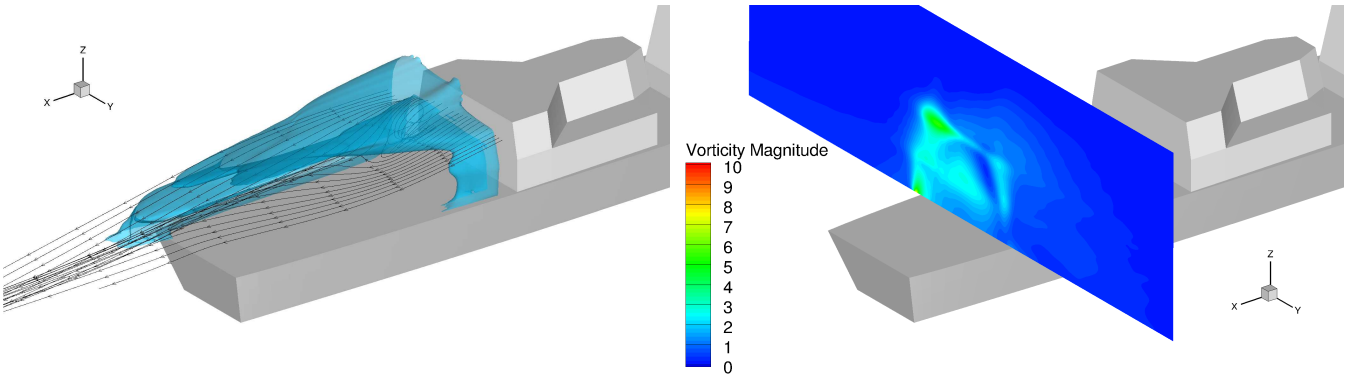

(a) Isolated ship wake

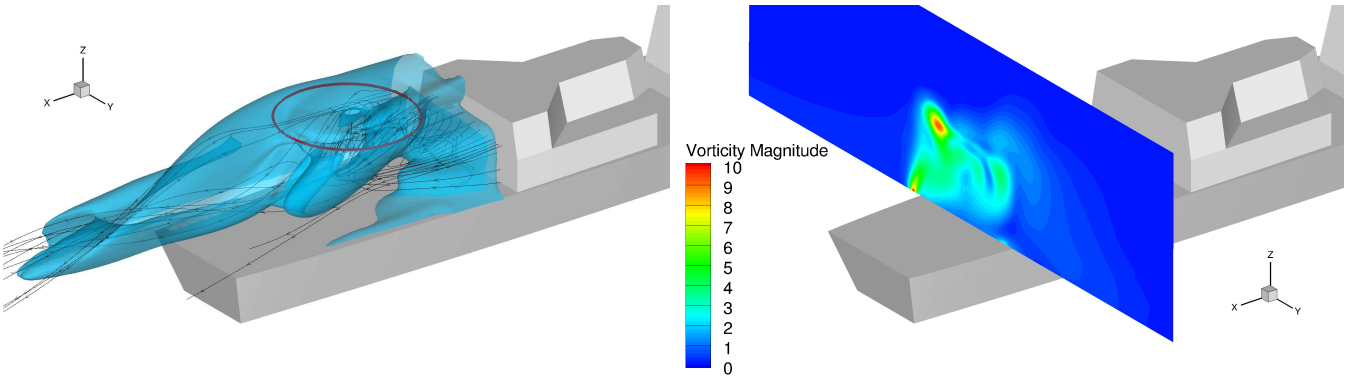

(b) Coupled simulation at $C_T^{UK} = 0.00734$

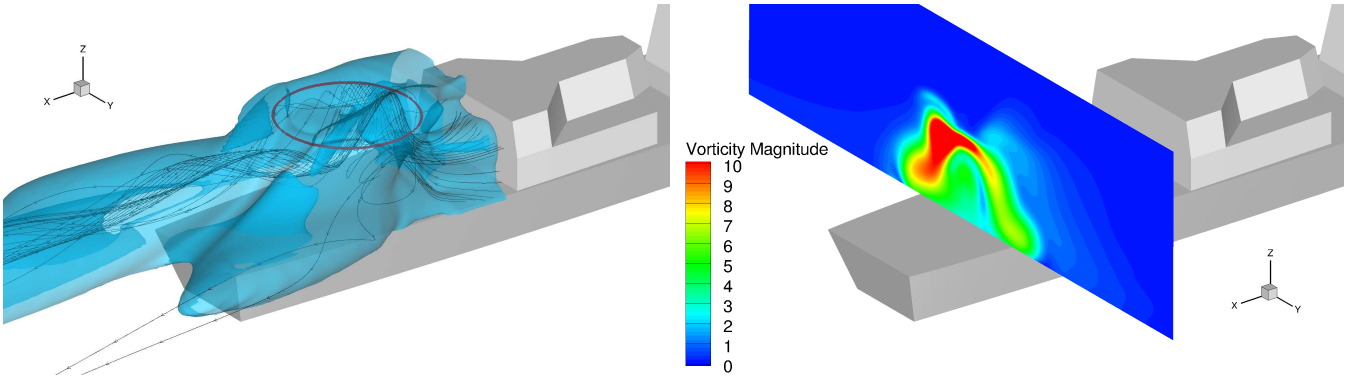

(c) Coupled simulation at $C_T^{UK} = 0.02936$

Figure 15: Iso-vorticity $\Omega_{mag} = 2$ and maps of vorticity at the back of the actuator disk of isolated ship and shipborne actuator disk at two different thrust coefficients, 12 degrees WOD

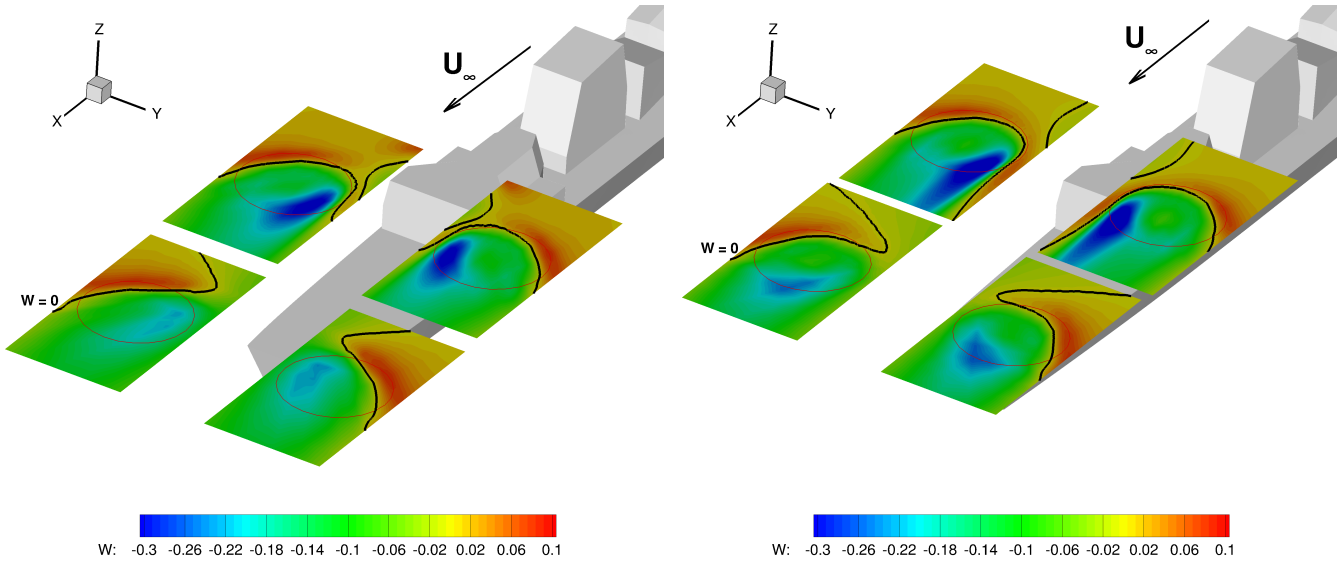

(a) 9 meters above deck

(b) 15 meters above deck

Figure 16: Contours of dimensionless velocity projected on a direction normal to the deck for 8 different positions of the actuator disk, at 0 degrees WOD.

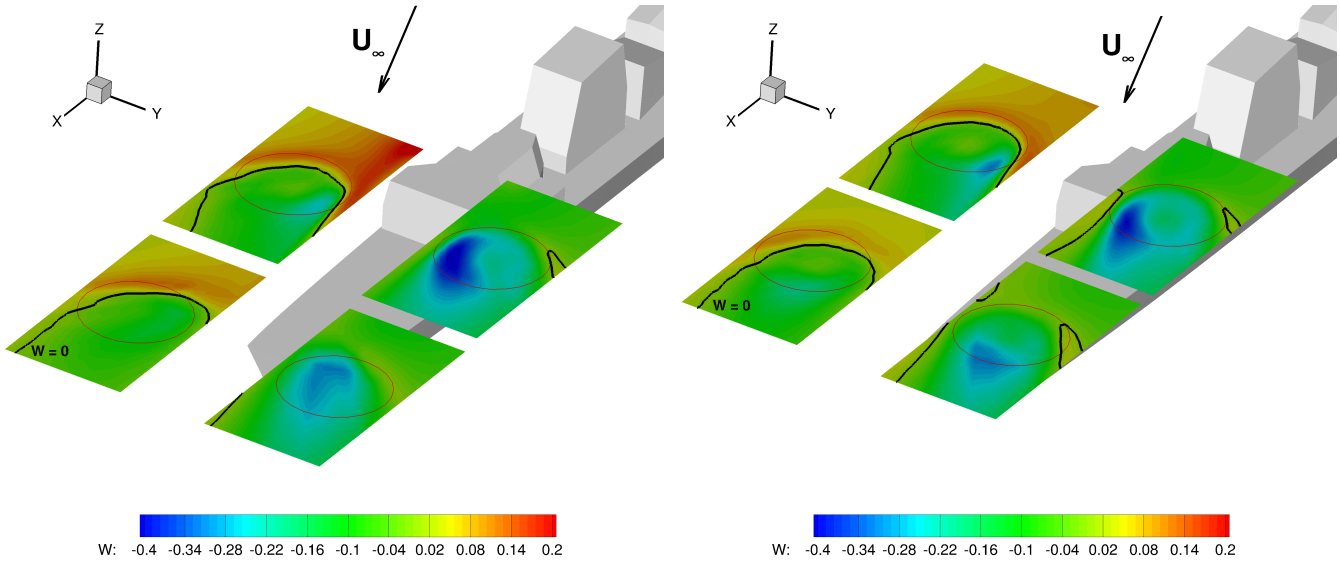

(a) 9 meters above deck

(b) 15 meters above deck

Figure 17: Contours of dimensionless velocity projected on a direction normal to the deck for 8 different positions of the actuator disk, at 12 degrees WOD.

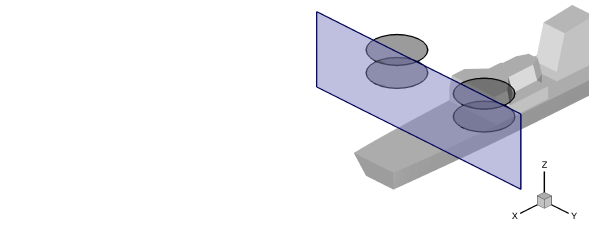

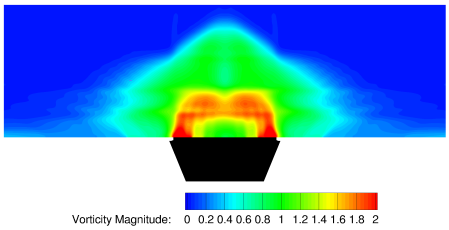

(a) Baseline, 0 degrees

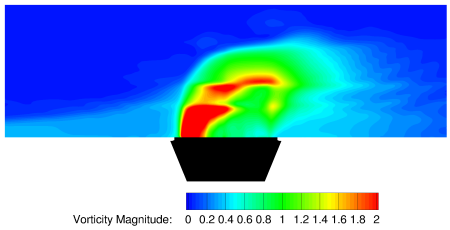

(b) Baseline, 12 degrees

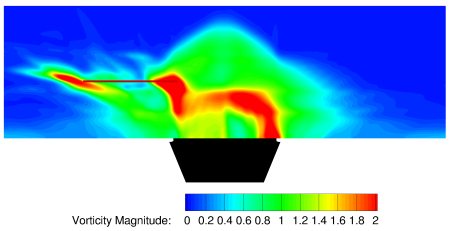

(c) 9 meters, portside, 0 degrees

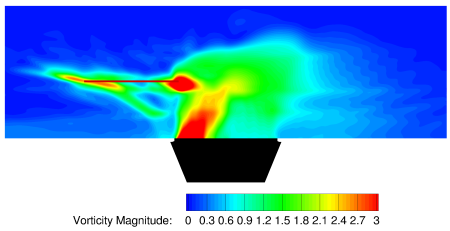

(d) 9 meters, portside, 12 degrees

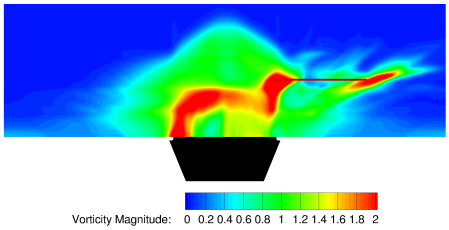

(e) 9 meters, starboard, 0 degrees

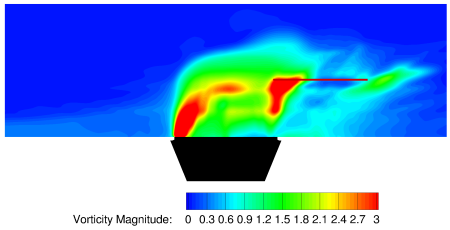

(f) 9 meters, starboard, 12 degrees

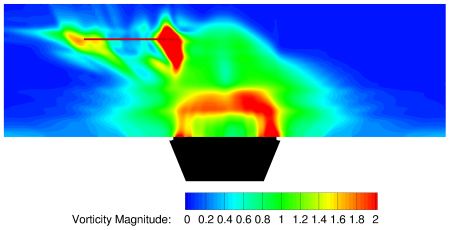

(g) 15 meters, portside, 0 degrees

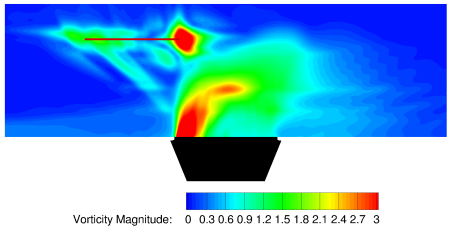

(h) 15 meters, portside, 12 degrees

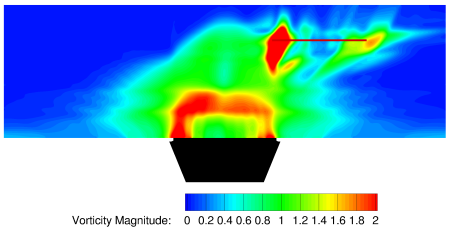

(i) 15 meters, starboard, 0 degrees

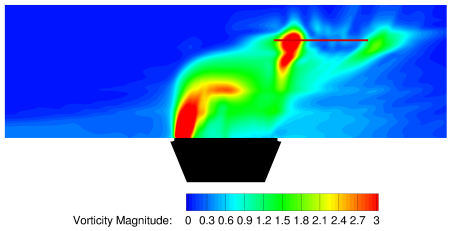

(j) 15 meters, starboard, 12 degrees

Figure 18: Maps of vorticity behind the ship for upstream cases. (a)(b) Baseline case (no actuator disk).

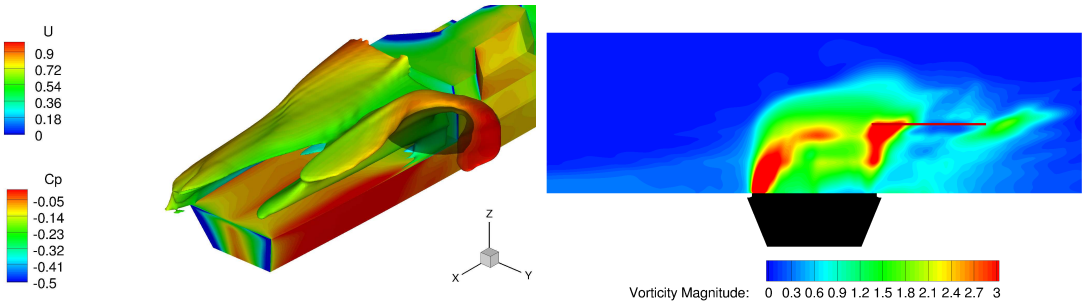

(a) $C_T^{UK} = 0.00734$

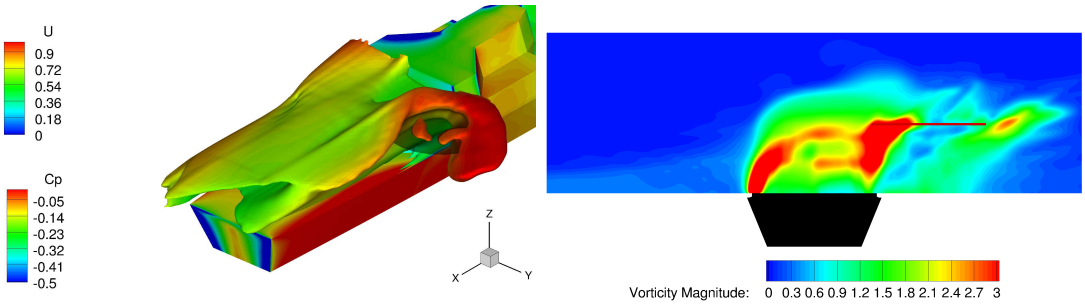

(b) $C_T^{UK} = 0.01468$

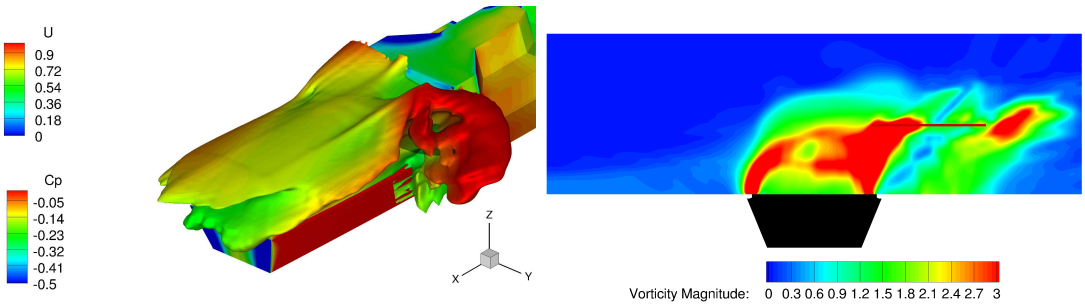

(c) $C_T^{UK} = 0.02936$

Figure 19: Maps of vorticity and iso-contours $\Omega_{mag} = 2$ behind the ship at the back of an upwind, leeward actuator disk at 9 meters above deck, 12 degrees WOD for 3 different thrust coefficients.

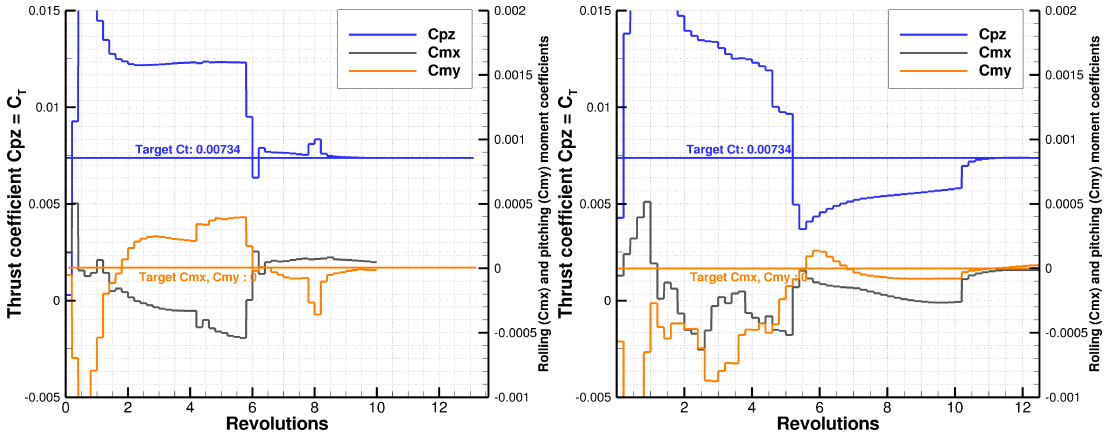

(a) Isolated rotor

(b) Shipborne rotor

Figure 20: Curves of thrust, pitch and roll moments coefficients used by the trimmer (average value over 1/5th of a revolution) for the isolated and shipborne rotors, compared with their respective target values.

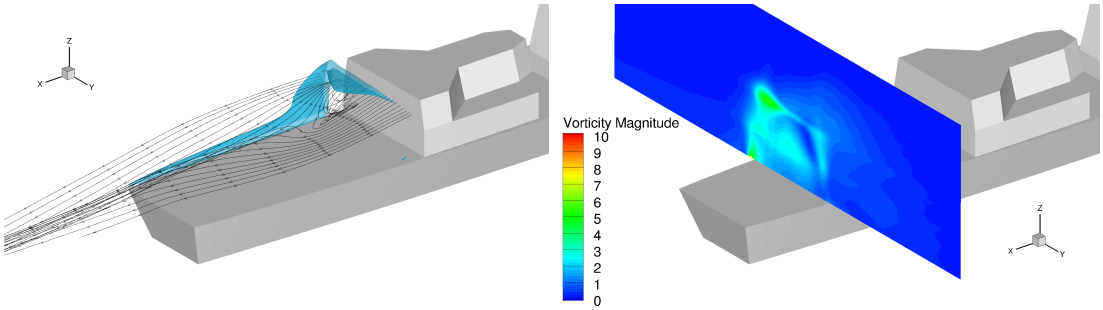

(a) Isolated ship

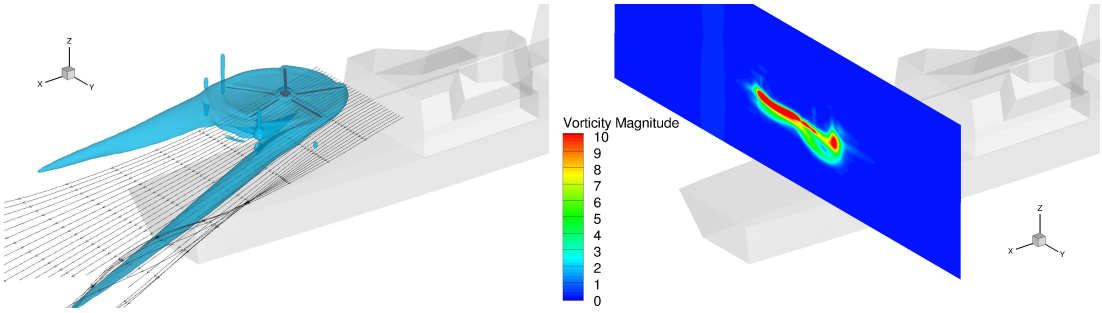

(b) Isolated rotor

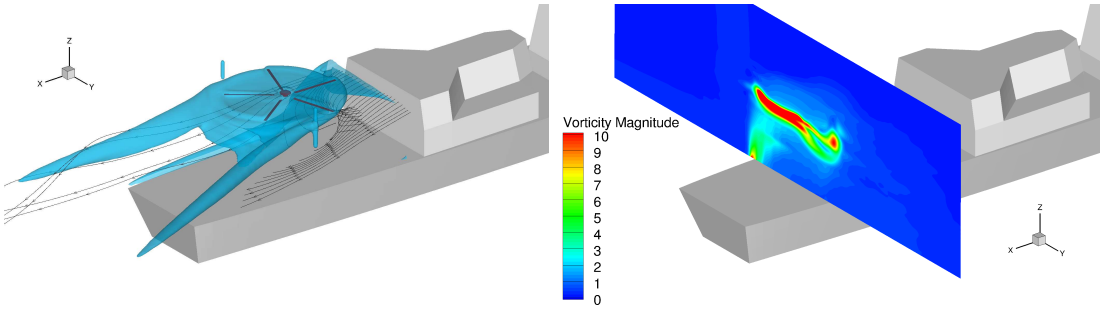

(c) Superposition

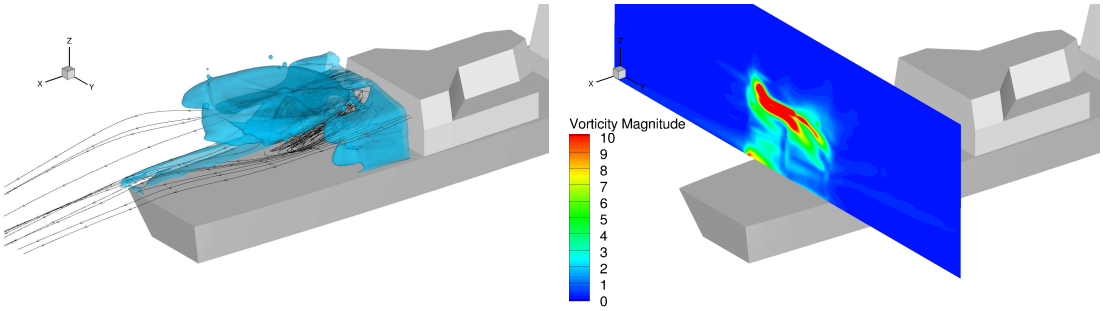

(d) Coupled

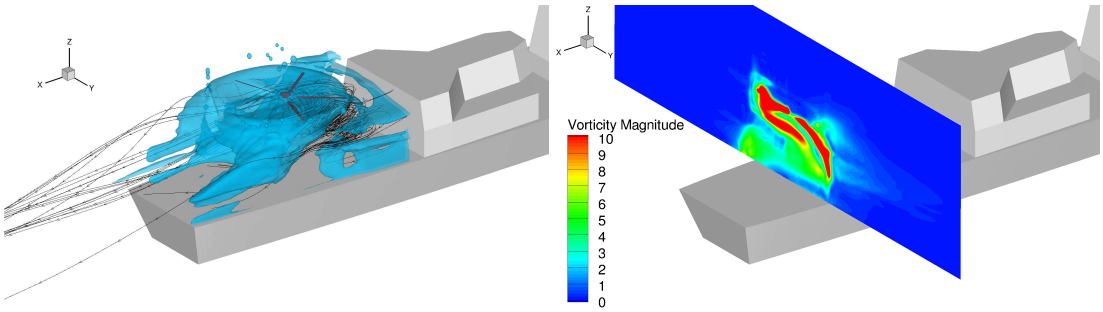

(e) Coupled at high thrust

Figure 21: Contours of iso-vorticity $\Omega_{mag} = 6$ with streamlines and maps of vorticity for isolated ship, isolated SeaKing rotor, superposition and coupled cases at 12 degrees WOD, $C_T = 0.00734$

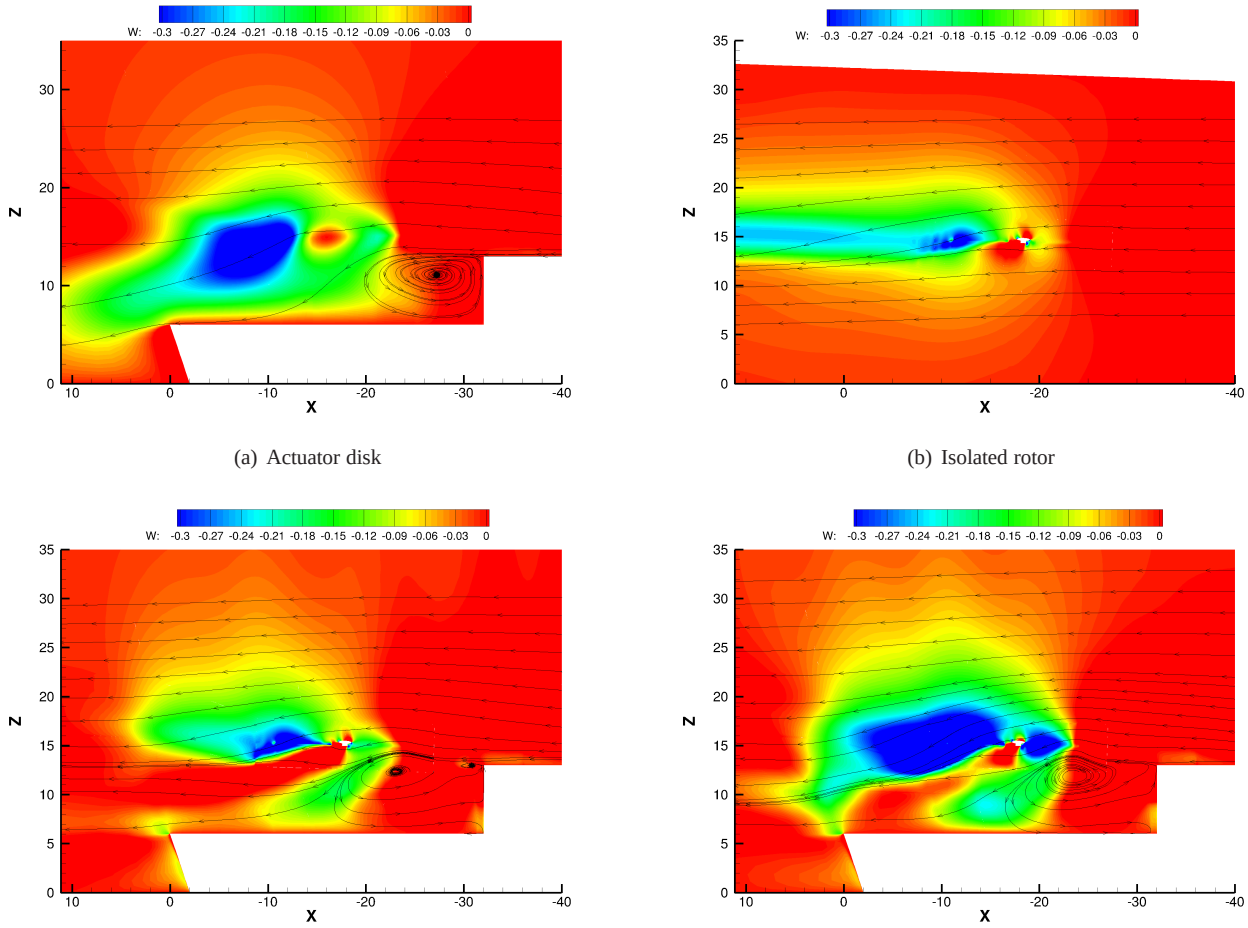

(a) Actuator disk

(b) Isolated rotor

(c) Shipborne rotor

(d) Shipborne rotor at high thrust

Figure 22: Slice of z-velocity normalised by the streamwise velocity with streamlines for actuator disk, isolated Sea-King rotor, shipborne rotor at $C_T^{UK} = 0.00734$ and shipborne rotor at $C_T^{UK} = 0.01468$.

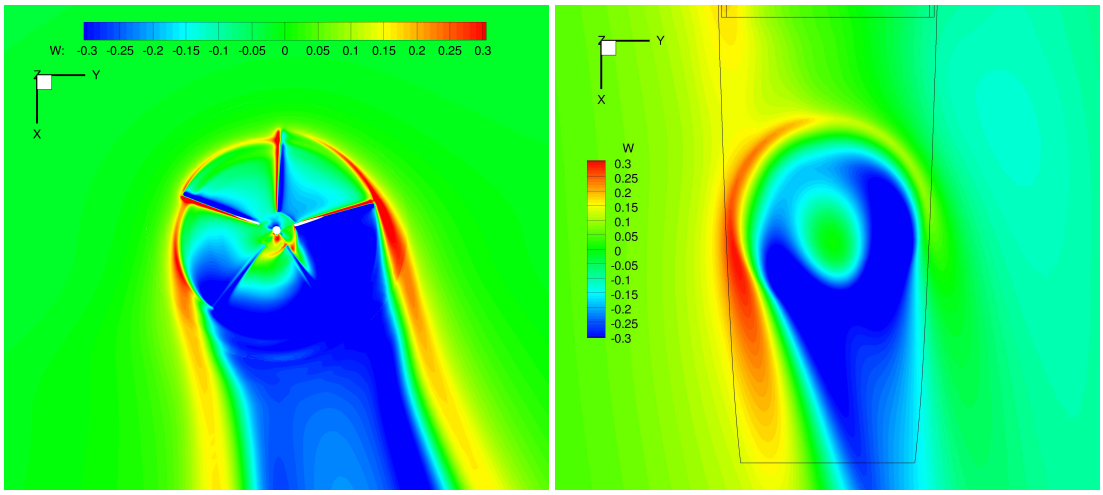

(a) Isolated SeaKing Rotor (b) Shipborne Actuator Disk

Figure 23: Maps of non-dimensional downwash velocity in a z-plane crossing the rotor disk. $C_T^{UK} = 0.00734$

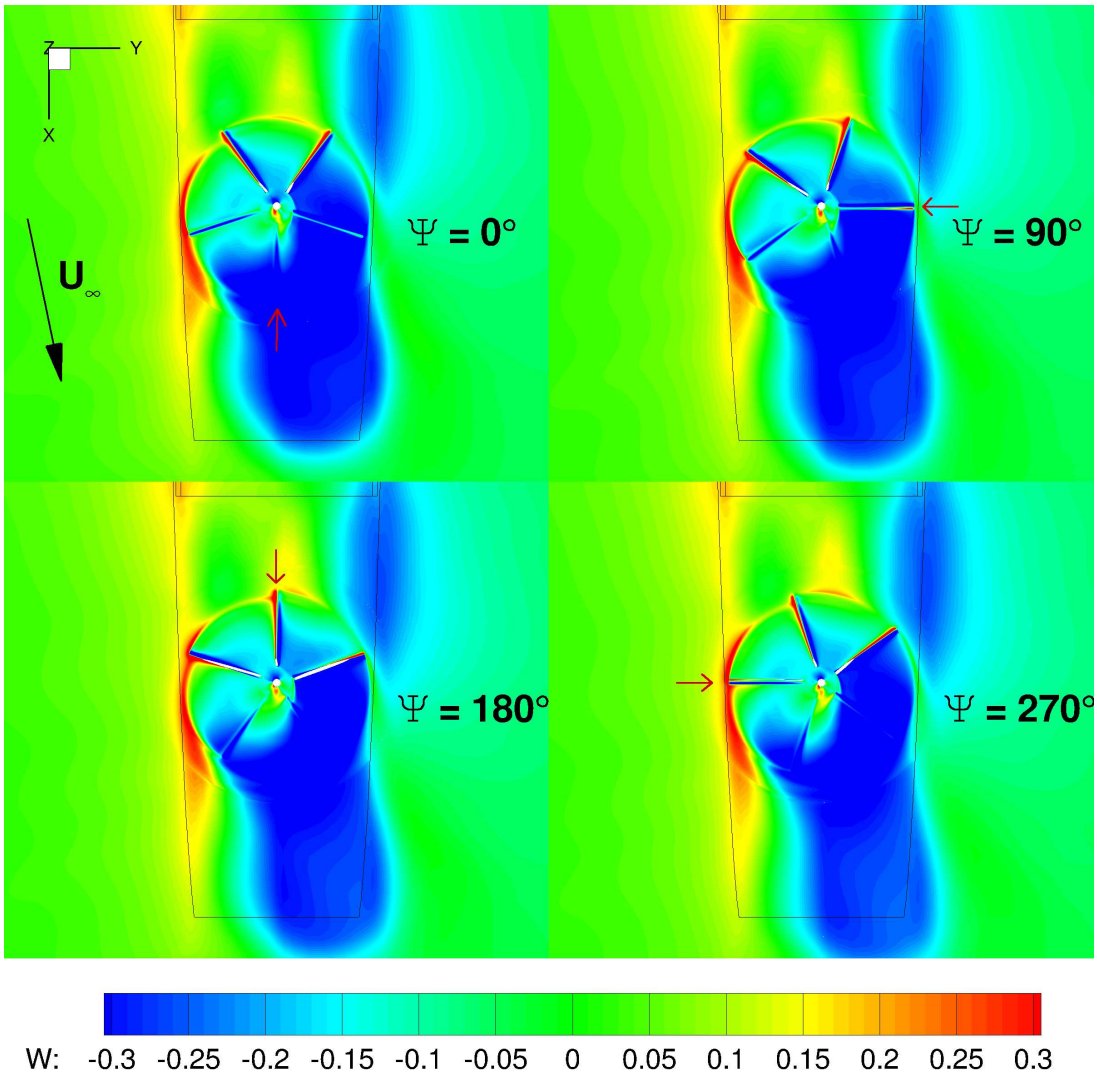

Figure 24: Maps of non-dimensional downwash velocity in a z-plane crossing the rotor disk. $C_T^{UK} = 0.00734$

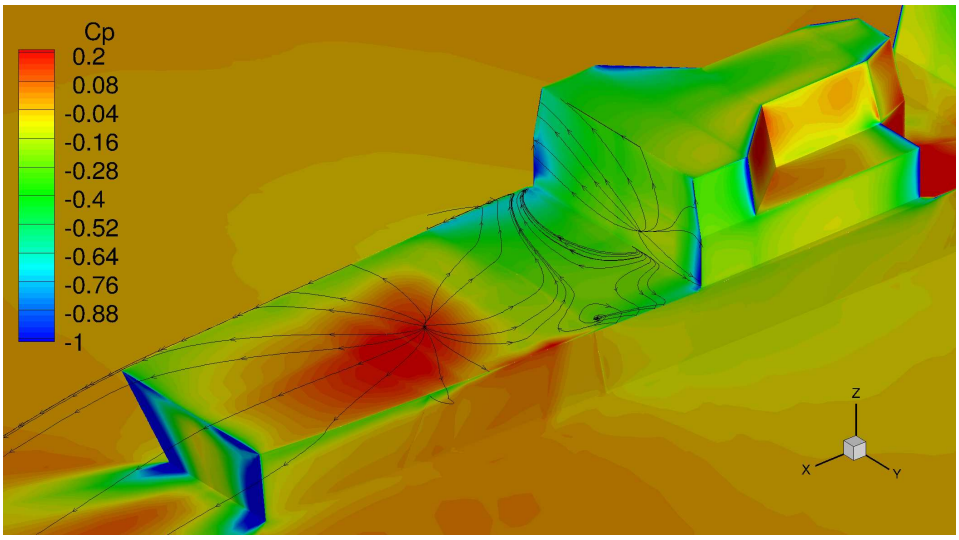

(a) Isolated ship

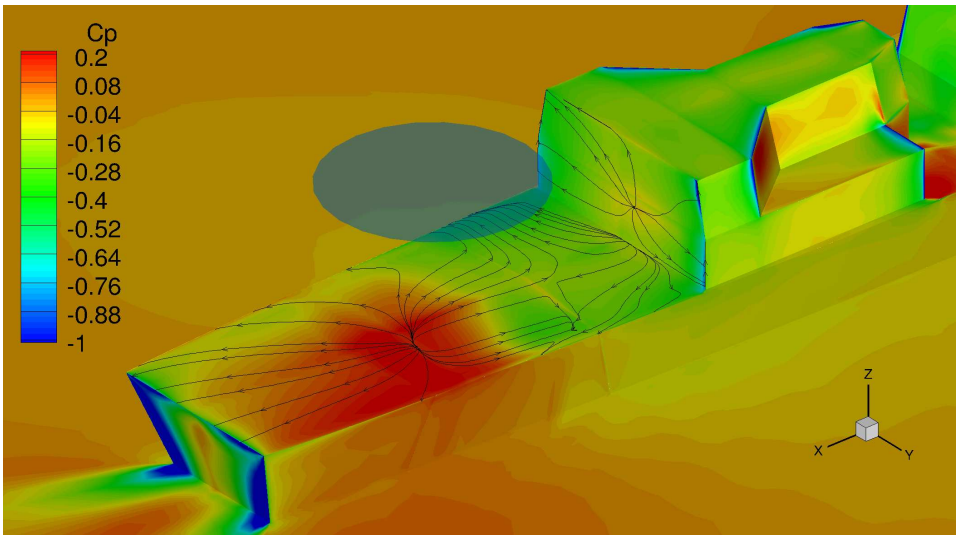

(b) Ship with SeaKing rotor at $C_T^{UK} = 0.00734$

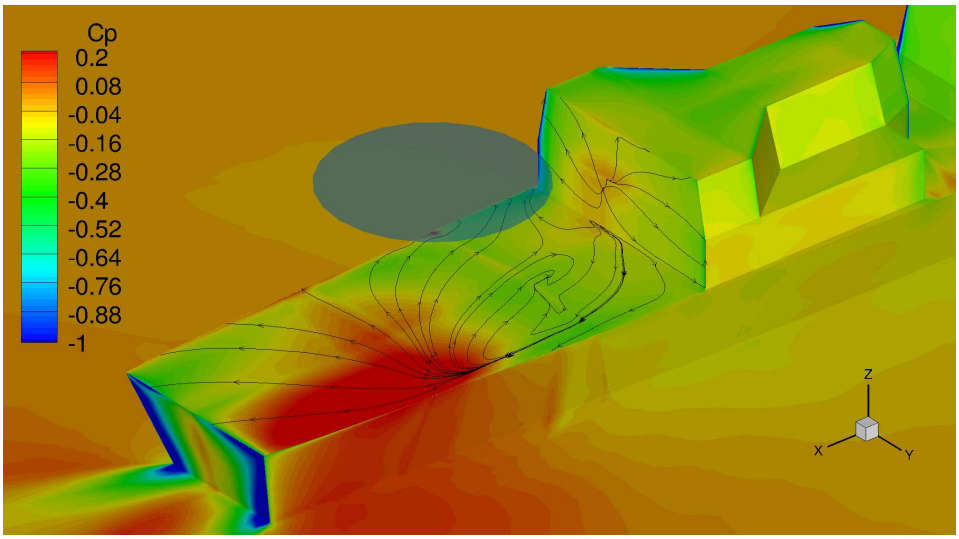

(c) Ship with SeaKing rotor at $C_T^{UK} = 0.01468$

Figure 25: Surface streamlines in the region of the deck for isolated ship and coupled case at two different thrust coefficients.

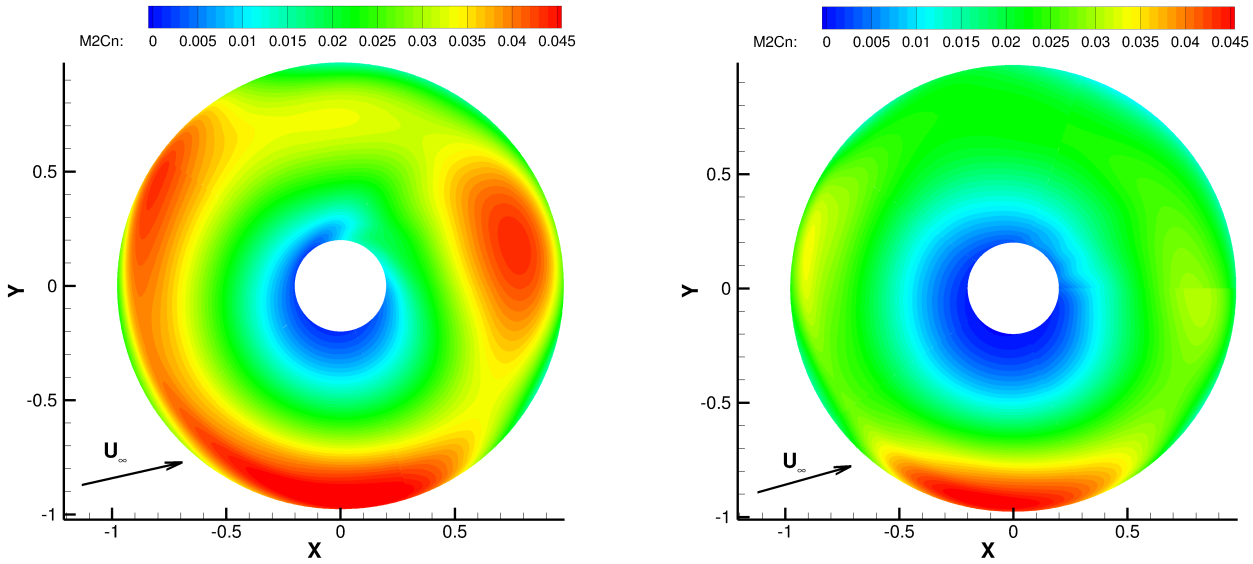

(a) Isolated rotor

(b) Shipborne rotor

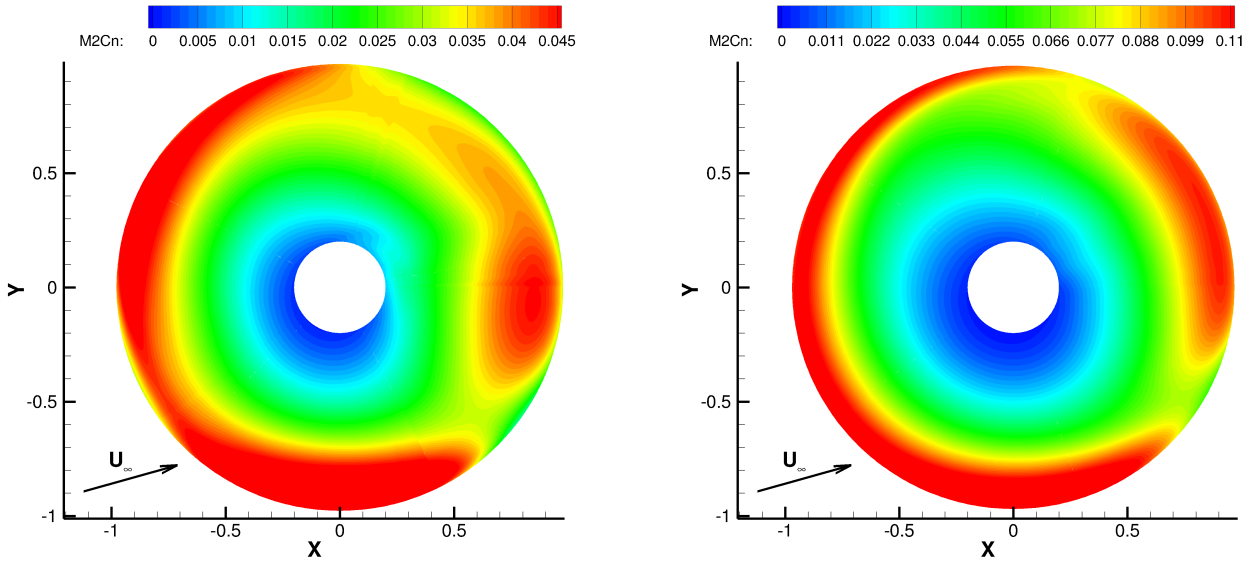

(c) Shipborne rotor $C_T^{UK} = 0.00734$

(d) Shipborne rotor $C_T^{UK} = 0.01468$

Figure 26: Normal force coefficient $M^2 C_N$ for (a) isolated rotor, (b) shipborne rotor and (c,d) shipborne rotor after retrimming for two thrust coefficients.

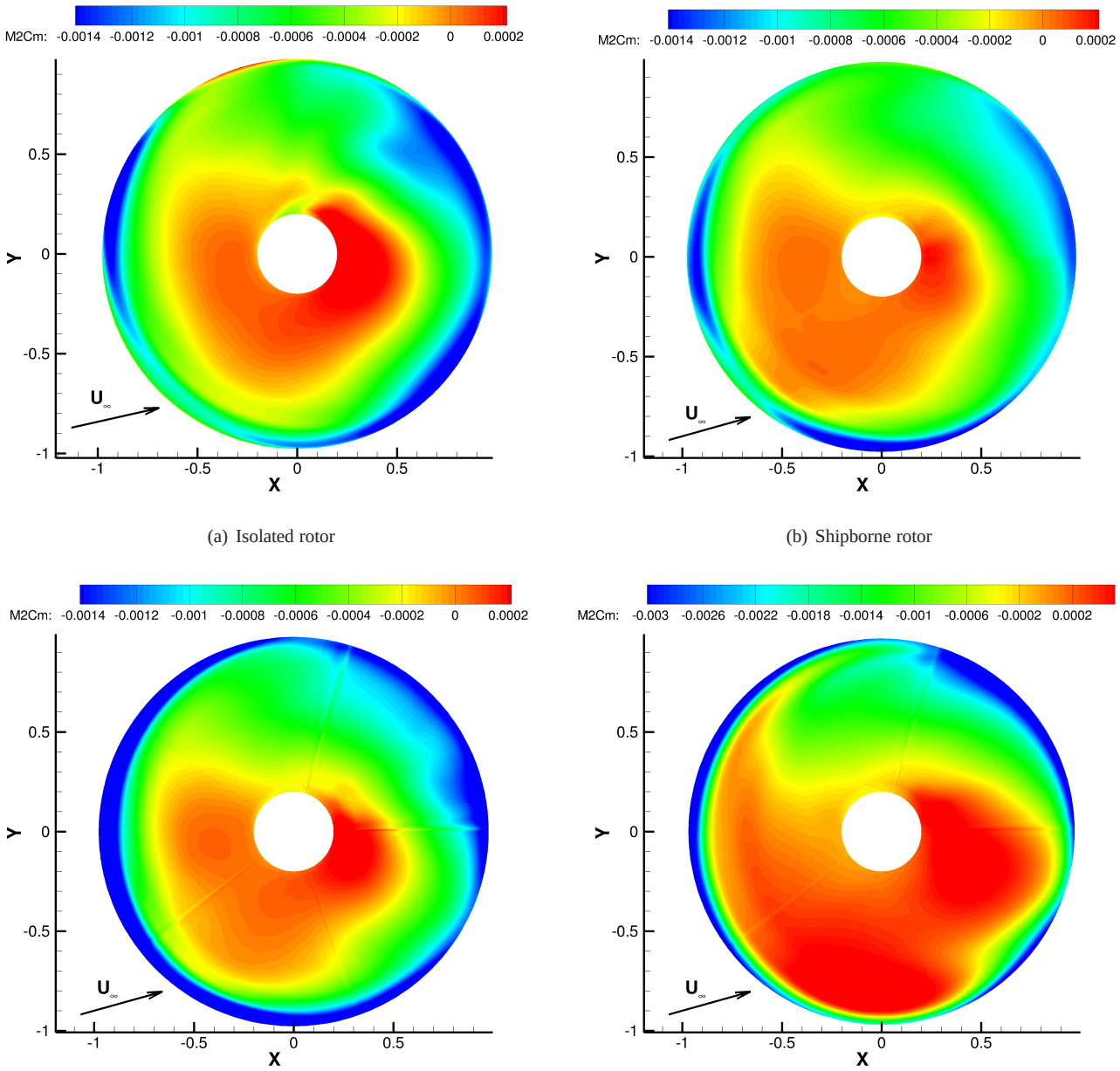

(a) Isolated rotor

(b) Shipborne rotor

(c) Shipborne rotor $C_T^{UK} = 0.00734$

(d) Shipborne rotor $C_T^{UK} = 0.01468$

Figure 27: Pitch moment coefficient $M^2 C_M$ for (a) isolated rotor, (b) shipborne rotor and (c,d) shipborne rotor after retrimming for two thrust coefficients.

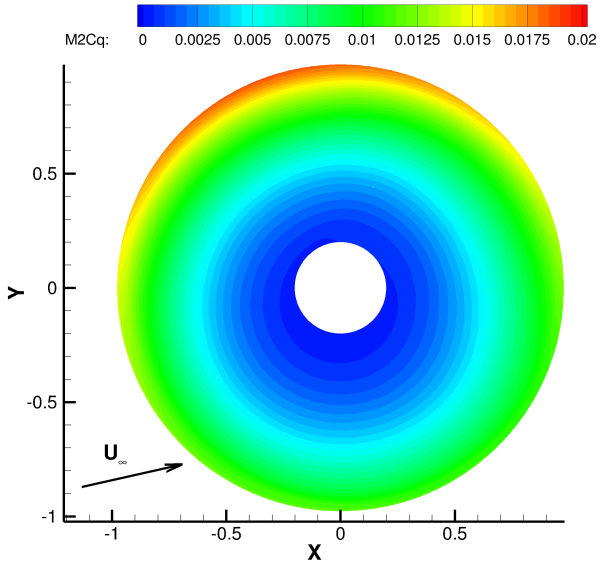

(a) Isolated rotor

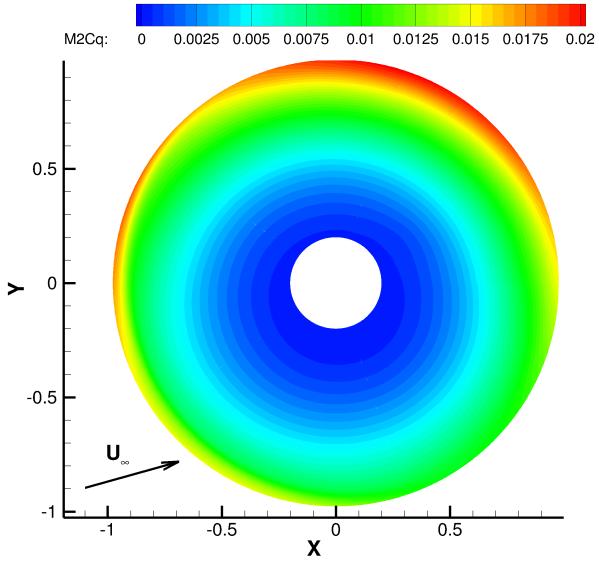

(b) Shipborne rotor

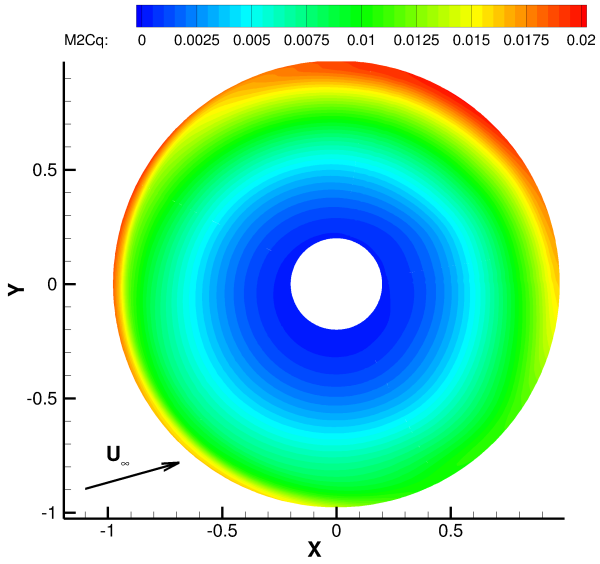

(c) Shipborne rotor $C_T^{UK} = 0.00734$

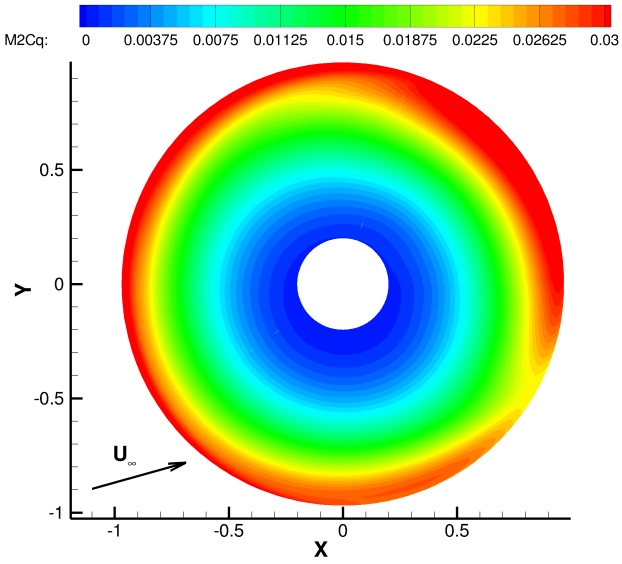

(d) Shipborne rotor $C_T^{UK} = 0.01468$

Figure 28: Torque coefficient M^2C_Q for (a) isolated rotor, (b) shipborne rotor and (c,d) shipborne rotor after retrimming for two thrust coefficients.

Authors	Year	Models	Grid size (in million cells)	Solver	Method
G.F. Syms [30]	2008	SFS2		PowerFlow	Lattice-Boltzmann - VLES.
J.S. Forrest *et al.* [5, 11]	2009-2010	SFS2, Type-23		Fluent	Finite-volume Navier-Stokes, DES turbulence model
G.F. Syms [29]	2004	CPF	0.9	CFD-ACE	Structured Navier-Stokes, steady, $k-\epsilon$ turbulence model
S.A. Polsky *et al.* [18]	2003	LHA	4	Cobalt	Unstructured Navier-Stokes, RANS and LES
N.H. Wakefield *et al.* [34, 35]	1999-2002	SFS		CFX	Navier-stokes 2D and 3D steady, Actuator Disk
G. Rajagopalan *et al.* [20]	2005	LHA, CH-46	3.4	Rot3DC	Unsteady Navier-Stokes, Actuator Disk
E. Alpman *et al.* [1, 3]	2007	LHA, UH-60	1.35 (hangar), 0.85 (LHA)	PUMA2 (CFD) / Genhel (flight dynamics)	Navier-Stokes URANS / BEM, Inflow model, Pilot model
Polsky *et al.* [17, 19, 31]	2006-2012	LHA, DDG, F-18, V22, JSF	10 to 29	Cobalt	Unstructured Navier-Stokes, LES, Actuator disk

Table 1: Summary of ship airwakes and shipborne rotors numerical studies

Authors	Year	Models	Experimental data
B.T. Cheney, S.J. Zan [4, 37]	1999-2001	1:100 SFS2 / 1:60 SFS1	Flow visualisation
Y.A. Nacakli *et al.* [15]	2011	1:50 SFS1 + four-bladed propeller	PIV measurements
R.G. Lee, S.J. Zan *et al.* [13, 14, 38, 40]	1999-2005	1:50 CPF, four-bladed rotor, Sea-King fuselage and rotor	Unsteady loads measurements
G.K. Yamauchi *et al.* [10, 20, 24, 33, 36]	2003-2005	1:48 LHA and V-22,CH-46,CH53 models	PIV and loads measurements.

Table 2: Summary of ship airwakes and shipborne rotors experiments

Variable	Exp. values	CFD		Full-scale values
		isolated rotor	ship and rotor	
Ship length	2.68 m	-	134.1	134.1 m
Ship beam	0.328 m	-	16.4	16.4 m
Rotor chord	$\approx$ 2 cm	1	0.344	0.5 m
Rotor diameter	28 cm	20.33	14.0	20.33 m
V_∞	19 m/s	1 (non-dim)	1 (non-dim)	$\approx$ 50 knots
Re_{meters}	1.3M	440,000	500,000	1.7M
Re_{beam}	424000	-	8.2M	28M
Re_{chord}	12,400	150,000	172,000	600,000
Re_{tip}	105000	1.27M	1.46M	5.0M
M_∞	0.055	0.055	0.055	$\approx$ 0.07
M_{tip}	0.466	0.466	0.466	$\approx$ 0.64
μ	0.118	0.118	0.118	0.118

Table 3: Comparison of flow conditions corresponding to wind-tunnel experiments, CFD calculations and full-scale equivalent.

Variable	Isolated rotor trim state	Shipborne rotor trim state	Difference
μ	0.118	0.118	
C_T^{UK}	0.00734	0.00734	
C_M^{pitch}	≈ 0	≈ 0	
C_M^{roll}	≈ 0	≈ 0	
C_Q	0.00162	0.00173	6.79%
θ_0	4.885	5.852	19.8%
θ_{1c}	-1.558	-1.596	
θ_{1s}	0.806	0.521	

Table 4: Values of the rotor characteristics after isolated and shipborne trimming.

Case	θ_0	θ_{1s}	θ_{1c}
Isolated rotor $C_T^{UK} = 0.00734$	4.885	0.806	1.558
Shipborne rotor $C_T^{UK} = 0.00734$	5.852	0.521	-1.596
Shipborne rotor $C_T^{UK} = 0.01468$	12.522391	1.656754	-3.241754

Table 5: Values of the estimated rotor trim states for the 2 values of C_T^{UK} tested.